



I Spy Transits and Pulsations: Empirical Variability in White Dwarfs Using Gaia and the Zwicky Transient Facility

Joseph A. Guidry¹ , Zachary P. Vanderbosch^{1,2} , J. J. Hermes³ , Brad N. Barlow⁴ , Isaac D. Lopez^{3,5} ,
Thomas M. Boudreaux⁶ , Kyle A. Corcoran⁷ , Keaton J. Bell^{8,11} , M. H. Montgomery^{1,2} , Tyler M. Heintz³ ,
Barbara G. Castanheira⁹ , Joshua S. Reding¹⁰ , Bart H. Dunlap¹ , D. E. Winget^{1,2} , Karen I. Winget^{1,2} , and J. W. Kuehne²

¹Department of Astronomy, The University of Texas at Austin, Austin, TX 78712, USA; josephguidry@utexas.edu

²McDonald Observatory, Fort Davis, TX 79734, USA

³Department of Astronomy, Boston University, 725 Commonwealth Avenue, Boston, MA 02215, USA

⁴Department of Physics, High Point University, High Point, NC 27268, USA

⁵Wentworth Institute of Technology, 550 W Huntington Avenue, Boston, MA 02215, USA

⁶Department of Physics and Astronomy, Dartmouth College, Hanover, NH 03755, US

⁷Department of Astronomy, University of Virginia, Charlottesville, VA 22904, USA

⁸DIRAC Institute, Department of Astronomy, University of Washington, Seattle, WA 98195, USA

⁹Department of Physics, Baylor University, Waco, TX 76798, USA

¹⁰Department of Physics and Astronomy, University of North Carolina at Chapel Hill, Chapel Hill, NC 27599, USA

Received 2020 November 30; revised 2021 February 26; accepted 2021 March 11; published 2021 May 12

Abstract

We present a novel method to detect variable astrophysical objects and transient phenomena using anomalous excess scatter in repeated measurements from public catalogs of Gaia DR2 and Zwicky Transient Facility (ZTF) DR3 photometry. We first provide a generalized, all-sky proxy for variability using only Gaia DR2 photometry, calibrated to white dwarf stars. To ensure more robust candidate detection, we further employ a method combining Gaia with ZTF photometry and alerts. To demonstrate its efficacy, we apply this latter technique to a sample of roughly 12,100 white dwarfs within 200 pc centered on the ZZ Ceti instability strip, where hydrogen-atmosphere white dwarfs are known to pulsate. By inspecting the top 1% of the samples ranked by these methods, we demonstrate that both the Gaia-only and ZTF-informed techniques are highly effective at identifying known and new variable white dwarfs, which we verify using follow-up, high-speed photometry. We confirm variability in all 33 out of 33 (100%) observed white dwarfs within our top 1% highest-ranked candidates, both inside and outside the ZZ Ceti instability strip. In addition to dozens of new pulsating white dwarfs, we also identify five white dwarfs highly likely to show transiting planetary debris; if confirmed, these systems would more than triple the number of white dwarfs known to host transiting debris.

Unified Astronomy Thesaurus concepts: White dwarf stars (1799); Variable stars (1761); Stellar pulsations (1625); ZZ Ceti stars (1847); Transits (1711); Planetesimals (1259); Circumstellar dust (236); Transient detection (1957); Cataclysmic variable stars (203)

1. Introduction

As astronomers prepare for the Vera C. Rubin Observatory and its Legacy Survey of Space and Time (LSST; Ivezić et al. 2019), we are entering an exciting era of big-data astronomy, with a rapid increase in synoptic photometric surveys that cover large areas of the sky. This shift is enabling astronomers to discover an exponentially increasing number of stars that go bump in the night.

Our understanding of white dwarf stars, which mark the endpoints of low- and intermediate-mass stars and their planetary systems, will benefit significantly from this new era (e.g., Fantin et al. 2020). The vast majority of white dwarfs are photometrically constant and make for excellent flux standards (Hermes et al. 2017a), but an important subset of these stellar remnants show photometric variability caused by a range of phenomena, including pulsations, binarity, surface inhomogeneities that rotate in and out of view, and more recently transits by both planets and planetary debris (Vanderburg et al. 2015; Vanderbosch et al. 2020; Vanderburg et al. 2020). Studying photometric variations in white dwarfs can therefore provide much insight into the end

stages of stars and planets. For example, the detection and characterization of these variations can enable the exploration of white dwarf interiors by means of performing asteroseismology on the pulsations present (e.g., Winget et al. 1994), or they could constrain the grain size and circumstellar dust properties of systems showing transiting debris (e.g., Hallakoun et al. 2017; Xu et al. 2019).

Searches for new pulsating white dwarfs have traditionally been focused on a narrow range in photometric color or spectroscopically determined effective temperature (e.g., Mukadam et al. 2004; Vincent et al. 2020). This is motivated by the fact that, as white dwarf stars cool monotonically throughout their lifetimes, they will eventually arrive at the ZZ Ceti instability strip, where hydrogen-atmosphere (DA) white dwarfs develop a deep enough convection zone to drive observable pulsations (Gianninas et al. 2015). ZZ Ceti typically exhibit optical variability, with peak-to-peak amplitudes of 1%–30% and periods ranging from 100 to 1500 s (Mukadam et al. 2013; Bognár et al. 2020).

Prior approaches to mining all-sky surveys for variable white dwarfs relied primarily on searches for coherent variability, manifesting as significant peaks in the periodograms of these noise-dominated, sporadically sampled observations (e.g., Rowan et al. 2019; Chen et al. 2020; Coughlin et al. 2020).

¹¹ NSF Astronomy and Astrophysics Postdoctoral Fellow.

These studies used variability metrics established upon finding significant periodicities in the Lomb–Scargle periodogram (Lomb 1976; Scargle 1982; see also VanderPlas 2018) computed from each object’s time-series photometry. Therefore, aperiodic photometric variations have so far mostly been neglected, despite the fact that the first pulsating white dwarf, HL Tau 76, was discovered from anomalous point-to-point scatter when observed for use as a flux standard (Landolt 1968). Similarly, Gaia DR2 catalogs of variables have mostly neglected short-term variable objects such as ZZ Ceti, since established periodic variability was required to flag a source as variable in Gaia DR2 (Holl et al. 2018).

Searches for other types of variability in white dwarfs have been less focused. Astronomers have unsuccessfully searched for transits from close-in planets or debris for more than a decade using large samples and wide-field surveys (e.g., Faedi et al. 2011; Fulton et al. 2014; van Sluijs & Van Eylen 2018; Rowan et al. 2019), as well as targeted searches around smaller samples (e.g., Sandhaus et al. 2016; Wallach et al. 2018; Dame et al. 2019; Brandner et al. 2021).

To date, only two white dwarfs have been observed to undergo transits from circumstellar debris: WD 1145+017, found from serendipitous K2 observations (Vanderburg et al. 2015); and ZTF J0139+5245 (Vanderbosch et al. 2020), found from serendipitous Zwicky Transient Facility (ZTF) photometry. Additionally, analysis of TESS data revealed transits from a companion straddling the planet/brown-dwarf boundary in a 1.4 day orbit around WD 1856+534 (Vanderburg et al. 2020).

Finding more white dwarfs with transiting circumstellar planetary debris will provide vital constraints on the dynamics and composition of planets and planetesimals during the final stages of stellar evolution (Farihi 2016). We expect that, as the host stars begin their evolution into white dwarfs, they will engulf any close-in planets out to roughly 1.5 au (Mustill & Villaver 2012), so the debris we see that survived this phase likely had its orbit perturbed inward toward the Roche limit of the white dwarf (e.g., Debes et al. 2012).

In the era of big-data astronomy, developing tools to efficiently mine all-sky surveys to discover more variable white dwarfs without computing periodograms should be prioritized, especially since white dwarfs offer the clearest window into the future and compositions of planetary systems. In this manuscript, we present two such methods that solely use anomalously high levels of scatter in Gaia DR2 and ZTF DR3 photometry as a proxy for variability.

The first is a global, all-sky proxy for variability that makes use of only Gaia DR2 photometry, while the second aims to build a more robust variability detection procedure through the inclusion of ZTF photometry and alerts. As a proof of concept, we applied the second method to a sample of 12,073 white dwarfs within 200 pc and centered on the ZZ Ceti instability strip, and confirm the detection of 19 new ZZ Ceti with follow-up high-speed photometry from McDonald Observatory. Additionally, we report robust evidence for five new white dwarfs that exhibit transit-like dips in their ZTF and/or McDonald light curves. We further discuss the potential for this method to expand the population of both pulsating white dwarfs and white dwarfs harboring transiting debris.

2. Observations

2.1. Gaia DR2 Photometry

We selected targets for variability assessment from the Gaia DR2 catalog of white dwarf candidates (Gentile Fusillo et al. 2019), which contains 486,623 objects. To ensure an astrometrically clean sample, we applied the quality cuts recommended by Lindegren et al. (2018) and Evans et al. (2018) (see Appendix A) and restricted our sources to those within 200 pc. This resulted in a list of 46,002 all-sky sources, which we use to assess variability using Gaia DR2 data products alone, with observations spanning 22 months from 2014 July to 2016 May (Gaia Collaboration et al. 2018).

From this 200 pc sample, we also generated a separate list of sources with photometrically determined effective temperatures near to or within the ZZ Ceti instability strip, where DA white dwarfs are found to pulsate. For this cut, we used the T_{eff} determinations provided by Gentile Fusillo et al. (2019), assuming H-atmospheres, and restricted the 200 pc sample to those with $7000 \leq T_{\text{eff}} \leq 16,000$. This sample forms the basis of our variability assessments using both ZTF and Gaia data products, so we also mandated all objects to have $15.0 \leq \text{PHOT_G_MEAN_MAG} \leq 21.0$ and $\text{DEC} > -25.0$, to stay within ZTF’s operational limits (Bellm et al. 2019). These cuts resulted in an object list with 18,269 sources.

2.2. Public ZTF Photometry

For the 18,269 objects defined in our sample centered on the ZZ Ceti instability strip, we queried the public ZTF survey (Bellm et al. 2019; Graham et al. 2019; Masci et al. 2019) for the DR3 g and r -band light curves by performing 3'' radii cone searches centered on the Gaia DR2 RA and DEC using the API provided by IRSA.¹² The coverage for ZTF DR3 extends from 2018 March 17 to 2019 December 31.

To remove any erroneous or potentially contaminated observations, we applied highly conservative filtering to these light curves. For every exposure, we required: $\text{catflags} = 0$, $|\text{sharp}| < 0.25$, and $\text{mag} < \text{limitmag} - 1.0$. The catflags and sharp constraints are both recommended cuts for clean light-curve extractions in the ZTF Science Data System Explanatory Supplement (ZSDS).¹³ We chose a slightly more restrictive cut on sharp than the recommended values of $|\text{sharp}| < 0.5$, to ensure better removal of elongated sources as well as those contaminated by cosmic rays. The constraint on limitmag was determined through trial and error after noting several objects that exhibited artificial flux increases when the measured magnitude was within 1.0 mag of an exposure’s limitmag .

Subsequently, we separated all of the light curves by filter type and sorted them by object ID (oid). Similarly to how we constructed the first limitmag constraint, we then discarded any observations where $\text{limitmag} - 1$ was less than the median observed magnitude for a respective oid and filter, to remove spuriously high flux measurements. To ensure the light curves queried at each Gaia source location all belonged to the same source, we compared the median ZTF g and r magnitudes for each oid to the cataloged Pan-STARRS1 (PS1) DR2 g - and r -band PSF-fit magnitudes. ZTF magnitudes are calibrated using PS1 photometry and generally agree within 0.10 mag out

¹² IRSA ZTF Light Curve Queries API

¹³ http://web.ipac.caltech.edu/staff/fmasci/ztf/ztf_pipelines_deliverables.pdf

to $g \approx 20$, $r \approx 20$ (Masci et al. 2019). If the median ZTF g and r magnitudes for a given oid differed from the respective PS1 magnitudes by more than 0.25 mag, any observations pertaining to such an oid were discarded to decontaminate the light curve from observations of neighboring objects. Moreover, only decontaminated light curves with at least 20 observations were considered in this analysis, i.e., $n_{\text{obs},g}$ or $n_{\text{obs},r} \geq 20$, to allow meaningful light-curve statistics and reduce the chance of including false-positive detections in our analysis (Chen et al. 2020).

Finally, we accessed the public ZTF transient alert database (Patterson et al. 2019) using the API provided by the Las Cumbres Observatory Make Alerts Really Simple (MARS) project¹⁴ to query alert packets for each of the 18,269 objects, granting us alert packets triggered from 2018 June 1 to 2020 August 4.

2.3. Final Object Sample and Decontamination

As a final decontamination check, we performed automated 1' cone search queries of PS1 photometry (Chambers et al. 2016; Flewelling et al. 2020) to identify any nearby objects that could contaminate both the Gaia DR2 and ZTF photometry with artificial excessive scatter, e.g., extremely bright stars or exceptionally close stars. We developed a system of empirically motivated criteria, similar to the ZTF light-curve filtering, to remove potentially contaminated objects from our catalog. These criteria are outlined in Appendix B.

After this automated decontamination step, we inspected the ZTF light curves and images for every object in our top 1% highest ranked sample (183 objects, not to be confused with the final top 1% presented in Section 4.2) by hand, to identify any remaining pathologies. We found several objects that had passed the PS1 search criteria in Appendix B but still had exceptionally close stars or nearby bright stars that were not cataloged by PS1. In addition, several objects exhibited large flux dropouts which, upon ZTF image inspection, were determined to be caused by bad pixel columns crossing the stellar PSF. Last, several objects near CCD edges were contaminated by unmasked ghosts, causing excess light-curve scatter. Such artifacts are expected, due to very bright stars that fall within CCD gaps or beyond the focal-plane edge (see Section 6.5 of the ZSDS).

In the end, the automated decontamination procedure flagged 4258 objects, and an additional 1926 objects lacked a sufficient number of ZTF observations, while the aforementioned inspection steps identified a total of 12 out of 183 contaminated objects in the top 1%. As a result, our final Gaia+ZTF sample contains a total of 12,073 objects.

2.4. Follow-up Observations

Over the course of two years, from 2018 October to 2020 November, we observed 34 white dwarfs in this study from McDonald Observatory on the 2.1 m Otto Struve telescope using the ProEM Camera at Cassegrain focus in order to obtain high-speed, time-series photometry to assess variability. While most observations were conducted using the blue broad-bandpass *BG40* filter, we obtained multicolor photometry for some objects using the SDSS g -, r -, and i -band filters. These 34 objects were originally identified as variable white dwarf

candidates based on excess Gaia photometric scatter (Equation (1)) and their triggering of ZTF transient alerts. In particular, objects with $T_{\text{eff}} \simeq 11,000$ K and $\log(g) \simeq 8.0$ were prioritized to see whether they pulsated at periodicities characteristic of outbursting ZZ Ceti (Bell et al. 2015, 2016; Hermes et al. 2015).

Following dark and flat-field corrections using standard IRAF procedures, we performed aperture photometry over a range of circular apertures using the CCD_HSP IRAF routine (Kanaan et al. 2002). Employing the Python package PHOT2LC (Z. P. Vanderbosch et al. 2021, in preparation),¹⁵ the light curves were sigma-clipped to 4σ using a moving window of width 25 data points, clipped by hand of clearly spurious data points, and detrended with a low-order polynomial fit to account for airmass changes. Within PHOT2LC, we used ASTROPY (Astropy Collaboration et al. 2013, 2018) to apply barycentric corrections to the mid-exposure time stamps of each image. The optimal aperture that minimized the average point-to-point scatter was selected for light-curve extraction. Light curves are presented in Appendix C with accompanying periodograms.

An additional eight white dwarfs were identified as variable candidates using the global Gaia variability metric. We observed these objects using the Small and Moderate Aperture Research Telescope System (SMARTS) consortium 0.9 m telescope at Cerro Tololo Inter-American Observatory in 2018 May. We obtained time-series photometry through a Johnson-V filter using the Tek2K CCD photometer at Cassegrain focus. These data were bias and flat-field corrected using standard IRAF routines. Aperture photometry was then conducted using the PHOTUTILS Python suite (Bradley et al. 2020) over a range of circular aperture radii. The light curves were sigma-clipped to 4σ , and the aperture that minimized the average point-to-point scatter was selected for analysis. These light curves and corresponding periodograms are presented in Appendix D along with a table of stellar parameters.

For some objects exhibiting variability indicative of transiting planetary debris or other nonpulsational phenomena, we obtained identification spectra using the second-generation Low-Resolution Spectrograph (LRS2; Chonis et al. 2016) on the 10.2 m Hobby-Eberly Telescope (HET) at McDonald Observatory. LRS2 is fed by a microlens-coupled bundle of 280 fibers, each 0.6 in diameter, with a unity fill factor over a $6'' \times 12''$ field of view. We used the blue LRS2 spectrograph (LRS2-B), which provides full coverage over 3700–7000 Å with two separate arms, UV and orange, overlapping between 4600 and 4700 Å. With two-point binning in the UV arm, we achieved spectral resolutions of about 4.4 and 5.1 Å in the UV and orange arms, respectively. We used LRS2-B to observe the transiting debris candidate ZTF J0923+4236 on 2020 November 2 with five consecutive 600-s exposures in 1.7 seeing, and to obtain time-resolved spectroscopy of the polar candidate ZTF J0146+4914 on 2020 November 7 with 13 consecutive 320 s exposures in 2.1 seeing. The spectra were reduced using the PANACEA reduction pipeline (G. Ziemann et al. 2021, in preparation).¹⁶

We also obtained follow-up observations using the DeVeny Spectrograph mounted on the 4.3 m Lowell Discovery Telescope (LDT, Bida et al. 2014). Using a 300 line mm⁻¹ grating and a 1'' slit, we obtained a roughly 4.6 Å resolution. Observations were carried out on 2020 November 16 with 1.7 seeing, with

¹⁴ <https://mars.lco.global/>

¹⁵ <https://github.com/zvanderbosch/phot2lc>

¹⁶ <https://github.com/grzeimann/Panacea>

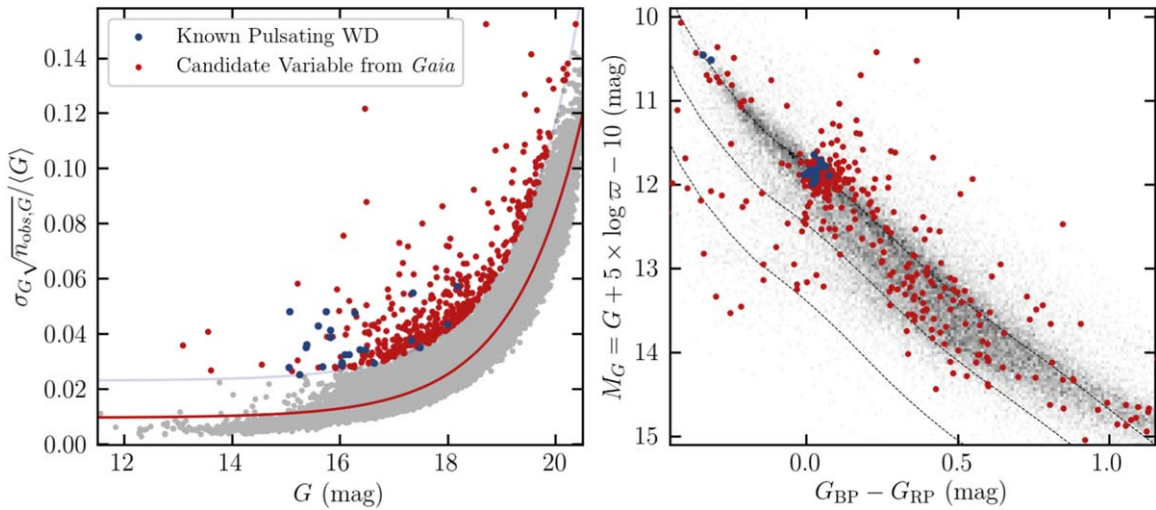


Figure 1. Left: empirical Gaia DR2 photometric variability metric as a function of magnitude for all white dwarfs in the 200 pc sample in gray. More details on the exponential fit are described in Appendix E. The 1% most variable white dwarfs are marked in red, and known pulsating white dwarfs in blue. Right: the 1% most variable white dwarfs defined at left are shown in the Gaia color–magnitude diagram. Dashed lines show hydrogen-atmosphere white dwarf cooling tracks from Tremblay et al. (2011) showing, from top to bottom, $\log(g) = 8.0, 8.5, 9.0$, corresponding to white dwarf masses of roughly $0.6, 0.9$, and $1.2 M_{\odot}$, respectively.

6×180 s exposures of ZTF J0328–1219 and 9×300 s exposures of ZTF0347–1802. Our spectra were debiased and flat-fielded using standard STARLINK routines (Currie et al. 2014), and were optimally extracted (Horne 1986) using the software PAMELA. Using MOLLY (Marsh 1989), we applied a wavelength and heliocentric correction.

3. Variability Metrics

3.1. Gaia Variability Metric

Our initial catalog of empirical white dwarf variability was constructed solely from observations released in Gaia DR2. We identified candidate variable white dwarfs by selecting white dwarfs with anomalously large photometric errors at a given reported mean magnitude (Hermes et al. 2018). Specifically, we employed Gaia’s broadband G -filter photometry (Evans et al. 2018), using the `PHOT_G_N_OBS`, `PHOT_G_MEAN_FLUX`, `PHOT_G_MEAN_FLUX_ERROR`, and `PHOT_G_MEAN_MAG` (henceforth $n_{\text{obs},G}$, $\langle G \rangle$, σ_G , and G , respectively) entries in particular. By definition, σ_G is an empirically determined value: the standard deviation of the G -band flux measurements normalized to $\sqrt{n_{\text{obs},G}}$ ¹⁷ (Carrasco et al. 2016; Evans et al. 2018). Therefore, σ_G is a quantification of the scatter in the Gaia photometry of individual sources (see also Eyer et al. 2020; Andrew et al. 2021; Mowlavi et al. 2021).

Our Gaia variability metric is shown in Figure 1 and defined as¹⁸:

$$V_G \equiv \frac{\sigma_G}{\langle G \rangle} \sqrt{n_{\text{obs},G}}. \quad (1)$$

The complicated scanning pattern that the Gaia spacecraft undertakes means some stars have been observed far more times than others, motivating us to normalize by the number of observations ($n_{\text{obs},G}$). The 22 months of photometry reported in Gaia DR2 has been iteratively clipped to 5σ (see Section 5.3.5 of the Gaia DR2 release documentation (Busso et al. 2018)), so

it is possible that the most variable white dwarf objects and systems are absent or underestimated by this metric. Still, objects with anomalously high σ_G values relative to similarly bright objects are candidates for excess scatter caused by variability.

To identify candidate variables, we use a double-exponential function (defined explicitly in Appendix E) to remove trends with magnitude and define our Gaia variability proxy, VARINDEX. The double-exponential, shown in light blue in the left panel of Figure 1, enables us to define the 1% most variable white dwarfs compared to this baseline. The position of these most-variable objects within the local (200 pc) sample of Gaia white dwarfs is shown in the right panel of Figure 1. The vast majority of variable objects are found near the ZZ Ceti (DAV) instability strip, where pulsations are known to cause high-amplitude optical variability, validating our method. Results when using this metric as a global proxy for variability are reported in Section 4.1.

Finally, we have constructed an additional Gaia DR2 variability metric, \tilde{V}_G , extended to our overlapping ZTF sample. Beginning with the raw V_G values obtained from Equation (1), we built this metric by first subtracting a sixth-order polynomial fit to the median V_G values within 50 iteratively sigma-clipped ($\sigma_{\text{upper}} = 3$, $\sigma_{\text{lower}} = 100$) magnitude bins of equal width using LMFIT (Newville et al. 2014); for a visualization, see the left panel of Figure 2. We then divided by an exponential fit to the standard deviation of the values in each bin, yielding the final Gaia DR2 variability metric, \tilde{V}_G , for our Gaia+ZTF sample.

3.2. ZTF Light-curve Metric

The ZTF light-curve metric is based on two measurements of excess scatter: the average point-to-point scatter (\tilde{V}_{P2P}) and the standard deviation in the normalized DR3 light curves (\tilde{V}_{SD}). Ultimately, whichever of the two metrics had the largest value was selected to represent the ZTF light-curve metric, \tilde{V}_{ZTF} , for an object: $\tilde{V}_{\text{ZTF}} \equiv \text{MAX}(\tilde{V}_{\text{SD}}, \tilde{V}_{\text{P2P}})$. This was intended to allow for the detection of both short- and long-term variability, so as not to avoid transient and transiting systems (see Section 5).

¹⁷ Gaia DR2 Data Release Documentation 14.1.1 GAIA_SOURCE

¹⁸ Equation (1) is identical to the Gaia DR2 variability proxy employed by Mowlavi et al. (2021).

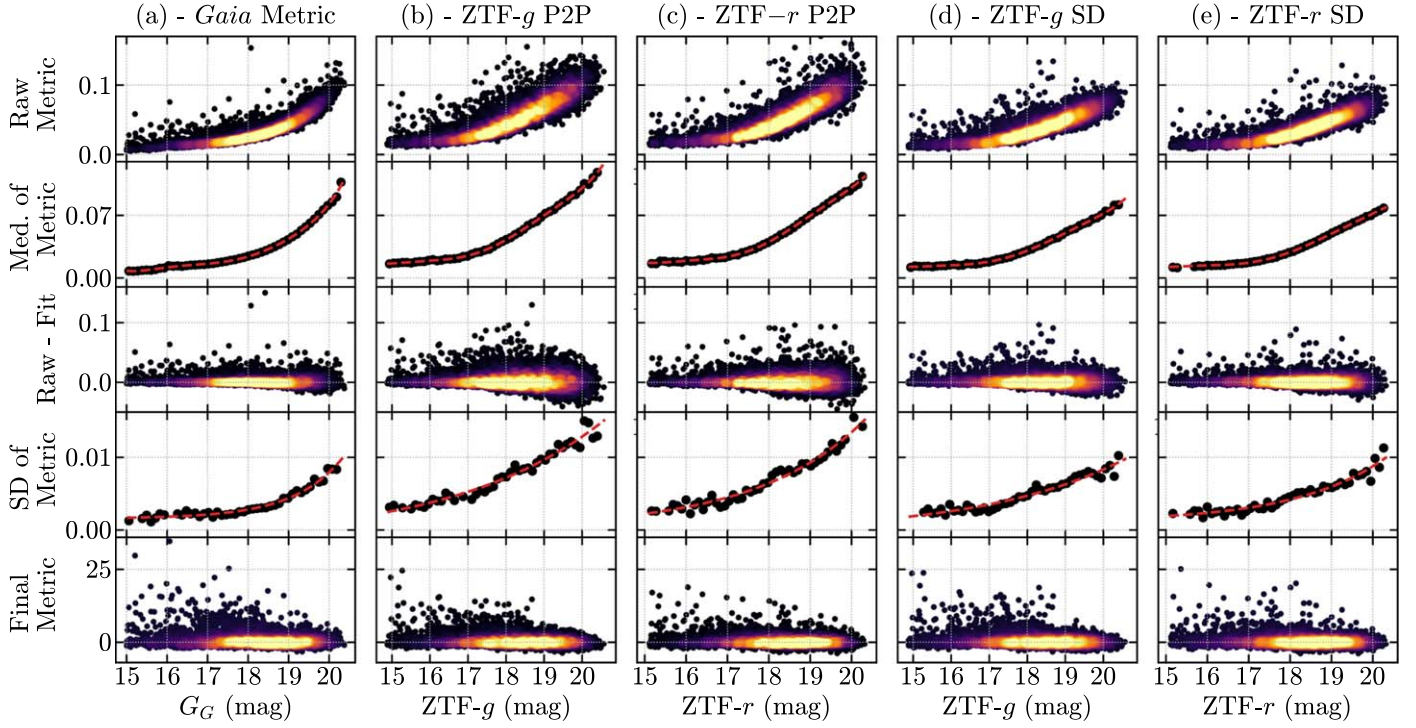


Figure 2. Visualization of the Gaia and ZTF point-to-point scatter (P2P) and standard deviation (SD) metrics, detailed in Sections 3.1 and 3.2. Each column pertains to an individual filter and metric, while each row catalogs the evolution of the metrics with each step in the detrending process, beginning with the raw metrics, then the fitted medians of the binned raw metrics, the differences between the above panels, the fitted standard deviations within each bin, and finally quotients of the above difference and fit. Distributions are color-coded such that brighter points indicate relatively dense regions, while dark points indicate sparse regions. Note that a small number of objects with exceptionally large metric values are not visible on these y-axis scales.

We applied an identical detrending routine to both the point-to-point scatter and standard deviation metrics independently, in order to remove trends with magnitude. First, we normalized each of the ZTF *g*- and *r*-band light curves to their respective median magnitudes, resulting in relative flux units, and then proceeded to calculate the raw *g* and *r* light-curve metrics. The raw metrics were then organized into 50 mag bins of equal width (covering $15.11 < r < 20.32$, with an average of 235 objects per bin) still separated by filter. This formed the four ZTF columns in Figure 2. After iteratively sigma-clipping each bin ($\sigma_{\text{upper}} = 3$, $\sigma_{\text{lower}} = 100$), we fit the median metric value of each bin with a sixth-order polynomial as a function of magnitude using the least-squares fitting Python module LMFIT. We subtracted this polynomial from the raw metrics to remove the trend in scatter with magnitude. This is visualized in the second and third rows of Figure 2.

Even with this polynomial subtraction, a trend in the standard deviations of the metrics with magnitude remained. To remove this second trend, we fit an exponential curve as a function of magnitude to the standard deviations of the metric values within the same magnitude bins from before using LMFIT, as depicted in row 4 of Figure 2. To ensure a high-quality fit, bins with fewer than five data points were excluded from this fitting procedure and outliers were removed by hand. The bins excluded in these fits were removed only to improve the fitting process, but the objects within them were not removed from our variability analysis. This prevented bins with poorly defined statistics from influencing the fitting process. We then divided the metric values by the fitted exponential to normalize the metrics onto scales of standard deviation (σ), yielding the distributions shown in the bottom row of Figure 2.

With the detrending complete, we combined the respective metrics from the ZTF-*g* and ZTF-*r* light curves into a single value through a weighted average normalized to the number of observations in each filter, yielding the final ZTF point-to-point scatter and standard deviation metrics, \tilde{V}_{P2P} and \tilde{V}_{SD} , respectively. Again, for each object, the larger of these two metrics was recorded as its final ZTF light-curve metric, \tilde{V}_{ZTF} .

3.3. ZTF Alert Metric

The ZTF Alert variability metric, N_A , is the number of alerts generated by an object that could be attributed to observations of real periodic or transient variability with high confidence. This was accomplished by filtering the alerts using a set of criteria outlined by the ZSDS and IPAC,¹⁹ where $rb \geq 0.65$, $n_{\text{bad}} = 0$, $\text{fwhm} \leq 5$ pixels, $\text{elong} \leq 1.2$, and $|\text{magdiff}| \leq 0.1$ mag.

Even though all observations that trigger alerts are already filtered by IPAC, these additional criteria construct a sturdy buffer that excludes any potentially false-positive observations.

3.4. Ranking Parameter

Capitalizing on the fact that \tilde{V}_G and \tilde{V}_{ZTF} are both set onto scales of σ , we defined a combined variability metric, R , that ranks objects according to their level of variability:

$$R = (\tilde{V}_G + \tilde{V}_{\text{ZTF}}) \cdot (1 + N_A). \quad (2)$$

Here, N_A serves as a boosting factor, rewarding objects that have triggered ZTF transient alerts, while not penalizing objects whose transient or periodic variability may be too low-

¹⁹ http://web.ipac.caltech.edu/staff/fmasci/ztf/ztf_pipelines_deliverables.pdf

Table 1
Sample Table of Parameters and Metrics for the Top 1% Most Variable White Dwarfs from Our Joint Gaia+ZTF Metrics

WD	α (deg)	δ (deg)	Class	R	\tilde{V}_{ZTF}	\tilde{V}_G	N_A	G	T_{eff}	$\log(g)$	Observed
WD J001038.25+173907.24	2.65952	17.65175	cZZ	27.7	4.1	9.7	1	17.8	11220	7.9	McD
WD J002511.11+121712.39	6.29599	12.28661	CV	139.7	9.8	25.2	3	17.5	8910	7.3	
WD J002535.80+223741.89	6.39950	22.62813	V	15.2	4.1	3.5	1	18.0	11490	8.1	
WD J004711.37+305609.18	11.79746	30.93552	cZZ	20.1	3.9	6.1	1	17.6	10450	7.5	ZTF
WD J010207.20−003259.57	15.53151	−0.55041	ZZ	14.6	3.3	11.3	0	18.2	10320	7.9	

Note. See Appendix F for the full table and description of columns.

amplitude to trigger alerts or whose ZTF coverage may have been too sparse for frequent detections of large flux changes. Likewise, by combining these individual metrics, we are able to rank variability in objects sampled over years of observations. The results pertaining to this ranking parameter are presented in Section 4.2, and a sample table of parameters from the top 1% most variable objects are found in Table 1.

4. Results

4.1. Top 1% Ranked Only by Gaia

The exquisite photometry collected by Gaia and released in DR2 has already revolutionized variability studies across the HR diagram, especially by Gaia Collaboration et al. (2019), who showed a high concentration of variable white dwarfs (>50%) around the ZZ Ceti instability strip. The ZZ Ceti instability strip is characterized by a narrow range of effective temperatures, since pulsations are only driven when the white dwarf develops a sufficiently deep convection zone.

However, reproducing the figures of Gaia Collaboration et al. (2019) poses a challenge, since most parameters (especially the G -band interquartile range) were not publicly released in Gaia DR2. A small handful of pulsating white dwarfs are flagged as “short-timescale variable” in Gaia DR2, but because the short-timescale (<1 day) variability processing was oriented toward sources with established periodic variability (Holl et al. 2018), there are rarely enough epochs to classify many variable or pulsating white dwarfs.

We show in Figure 1 a remarkable consistency with Gaia Collaboration et al. (2019) using our VARINDEX and Gaia variability metrics, especially the regions of the Gaia color-magnitude diagram with the most-variable white dwarfs. The biggest clustering of variables in both cases occurs near the colors²⁰ of the ZZ Ceti instability strip, near $G_{\text{BP}} - G_{\text{RP}} = 0.0$ mag and $M_G = 12.0$ mag.

Nearly one-quarter (23) of the 99 known pulsating white dwarfs within 200 pc (Bognar & Sodor 2016) meet our criterion for the 1% most variable white dwarfs by having a VARINDEX >0.0074 (see Appendix E). We have followed up a number of white dwarfs that are without previous mention in the literature and have the largest Gaia VARINDEX, using high-speed photometry, especially from CTIO in the Southern Hemisphere, and we confirm eight new pulsating white dwarfs. All are detailed in Appendix C.

Our double-exponential calibration should define any object with VARINDEX >0.0 as a strong candidate for variability: this value is met by 1423 (3%) of white dwarfs within 200 pc. This fraction is similar to the results of Hermes et al. (2017a), who show from Kepler and K2 observations that (>97%) of

nonpulsating and apparently isolated white dwarfs are photometrically constant to better than 1% in the Kepler bandpass on 1 hr to 10 day timescales. Nearly 40% (38) of the previously known pulsating white dwarfs within 200 pc have VARINDEX >0.0.

Our full implementation of the VARINDEX is likely valid to select variables for any objects in the magnitude range $13 < G < 20$ mag, and is described in full in Appendix E. We also report a calibration of this metric to Gaia Early Data Release 3, VARINDEX_{EDR3}, in Appendix E. Further sections outline our attempts to improve variable white dwarf selection by pairing Gaia DR2 with ZTF DR3 empirical variability.

4.2. Top 1% Ranked by Gaia+ZTF

Out of the ensemble of roughly 12,100 objects with reliable Gaia and ZTF photometry, we only explored the top 1% most variable objects in this study, objects with $R \geq 12.9$, as these objects can be assigned a high confidence of being variable. Reassuringly, a literature search using SIMBAD revealed 41 of these 121 objects to be known variable white dwarf systems, including ZZ Ceti, cataclysmic variables, eclipsing binaries, and the two known transiting debris systems. These known variables are distributed evenly throughout the sample, with rankings as high as 3 and as low as 118.

The remaining 86 objects were either unstudied objects or not previously known to be variable. We obtained follow-up, high-speed photometry from the 2.1 m Otto Struve telescope at McDonald Observatory for 33 of these objects found in this top 1% subset, and all revealed variability, mostly indicative of ZZ Ceti pulsations. Six of these objects were recently confirmed to be ZZ Ceti (Vincent et al. 2020), further supporting our selection criteria. Furthermore, while two of these 33 objects do not demonstrate short-term variability, they clearly demonstrate long-term variability in their ZTF photometry. All 121 objects are presented in the table in Appendix F, while a sample of this information is presented in Table 1.

A categorical breakdown of the top 1% is shown in Table 2 and further reflected in Figure 3. Most of these objects reside inside the ZZ Ceti instability strip, of which the overwhelming majority are known and candidate ZZ Ceti. Outside the empirical boundaries of the instability strip are mostly nonpulsating objects, such as known and candidate cataclysmic variables, eclipsing binaries, and transiting planetary debris systems. We specifically review our classifications of new candidate transiting debris systems and ZZ Ceti in Sections 5 and 6, respectively.

Figure 4 further captures the diversity of the top 1%, showcasing two white dwarfs clearly exhibiting variability not indicative of pulsations—(a) ZTF J0107+2107 and (b) ZTF J0146+4914—and two pulsating ZZ Ceti, (c) WD J0433+4850, a known ZZ Ceti (Vincent et al. 2020), and (d) SDSS J1106+1802. This figure shows the ability of our method to translate objects with excess

²⁰ <http://www.astro.umontreal.ca/~bergeron/CoolingModels/>

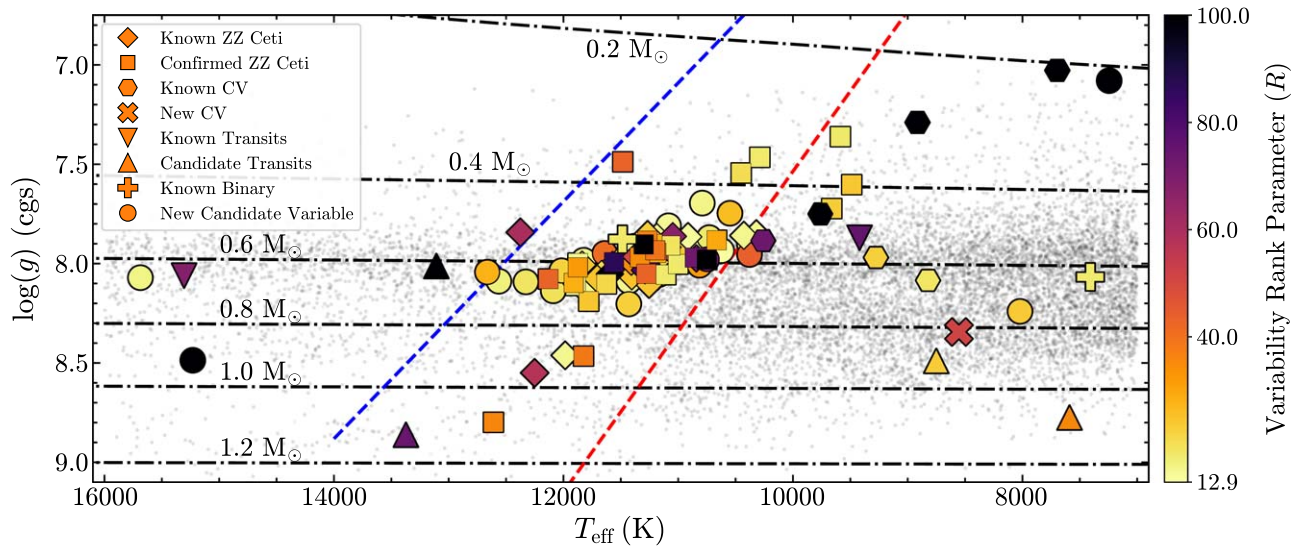


Figure 3. Photometrically determined temperature and surface gravity of our sample, with the top 1% color-coded by their variability rank parameter value, R . Red and blue dashed lines indicate the empirical cool and hot boundaries of the ZZ Ceti instability strip (Gianninas et al. 2015), while dashed-dotted black horizontal lines trace theoretical evolutionary cooling tracks for various masses (Tremblay et al. 2011). The vast majority of our highest-ranked objects are concentrated within the ZZ Ceti instability strip, but numerous nonpulsating variables are found at different temperatures, especially new candidate and known white dwarfs hosting transiting planetary debris. We plot the remainder of our sample as faint black circles in the background.

Table 2

Classification of the Top 1% Most Variable Objects from the Gaia+ZTF Metrics

Object Type	Number
ZZ Ceti	31 known, 29 new confirmed
Cataclysmic Variable	6 known, 1 new candidate
Eclipsing Binary	2 known
Transiting Debris	2 known, 4 ^a new candidates
Magnetic Spot	1 new candidate
Unconfirmed Variable	45 new candidates

Note.

^a An additional object ranked in the top 1% from our Gaia-only method also appears to have transit-like dips on short timescales in its follow-up McDonald 2.1 m photometry (Section 5).

scatter in their ZTF photometry in the left panels into real detections of variability in the follow-up time-series observations. As best demonstrated by the bottom two objects, by relying on excess photometric scatter instead of searching for significant periodogram peaks, we are able to identify both nonperiodic and short-period variable white dwarfs that would otherwise go undetected at the typical sampling rates of Gaia and ZTF. In doing so, our method is sensitive to variability on timescales ranging from minutes to days.

While our variability ranking metric does not include an assessment of the periodograms of ZTF light curves, we still performed a search for significant periodicities within the ZTF data of the top 1%, to aid in the classification of candidate variables lacking ground-based follow-up. We first applied barycentric corrections to the ZTF time stamps before proceeding to compute the Lomb–Scargle periodogram of the g , r , and combined $g+r$ light curves. We then searched for any signals greater than four times the mean amplitude ($4\langle A \rangle$) of the respective periodograms. For this exercise, all periodograms were computed over a grid of frequencies ranging from 1–5000 μHz , oversampled by a factor of twice the light-curve

baseline. We also excluded frequencies equivalent to 0.95–1.05 and 0.48–0.52 cycles per day, to reject aliases of the typical diurnal sampling rate (Coughlin et al. 2020). This returned 81 out of 121 objects showing periodic variability beyond the $4\langle A \rangle$ significance threshold.

Considering the elevated noise from the long baselines and typical long-cadence mean sampling rates of the ZTF time series, we then computed more conservative 0.1% false alarm probability significance thresholds for each of these 81 objects. To estimate these significance thresholds, we used a bootstrap method (see VanderPlas 2018; Bell et al. 2019), where the combined $g+r$ flux measurements were randomly resampled 10,000 times with replacement using ASTROPY. We then computed the maximum amplitude values of the Lomb–Scargle periodogram for each bootstrapped light curve, keeping the original time stamps for each iteration. The 99.9th percentile of the distribution of maximum amplitudes is then assumed as the 0.1% false alarm probability level. The mean of the 81 computed significance thresholds was found to be a factor of 4.94 ± 0.23 times the original periodogram amplitudes, justifying the adoption of a significance threshold of $5\langle A \rangle$ in future analyses in order to avoid such a computationally expensive procedure.

A final search for significant peaks was then performed on the original light curves using these computed significance thresholds. So as not to count artificial signals from the wide spectral window, we imposed a $\pm 50 \mu\text{Hz}$ buffer around each peak. This buffer was widened to $100 \mu\text{Hz}$ for objects densely observed at short cadences during at least one night, to account for the exaggerated spectral window effects. An automated recursive prewhitening routine was performed to optimize the selection of significant frequencies using least-squares fitting and minimization of summed sinusoids with LMFIT. To remove combination frequencies and harmonics, we identified any frequencies that agreed to within the respective $50 \mu\text{Hz}$ or $100 \mu\text{Hz}$ window of a sum, difference, or integer multiple between any signals of greater amplitude. As a result, we report 26 objects in the top 1% exhibiting significant periods in either

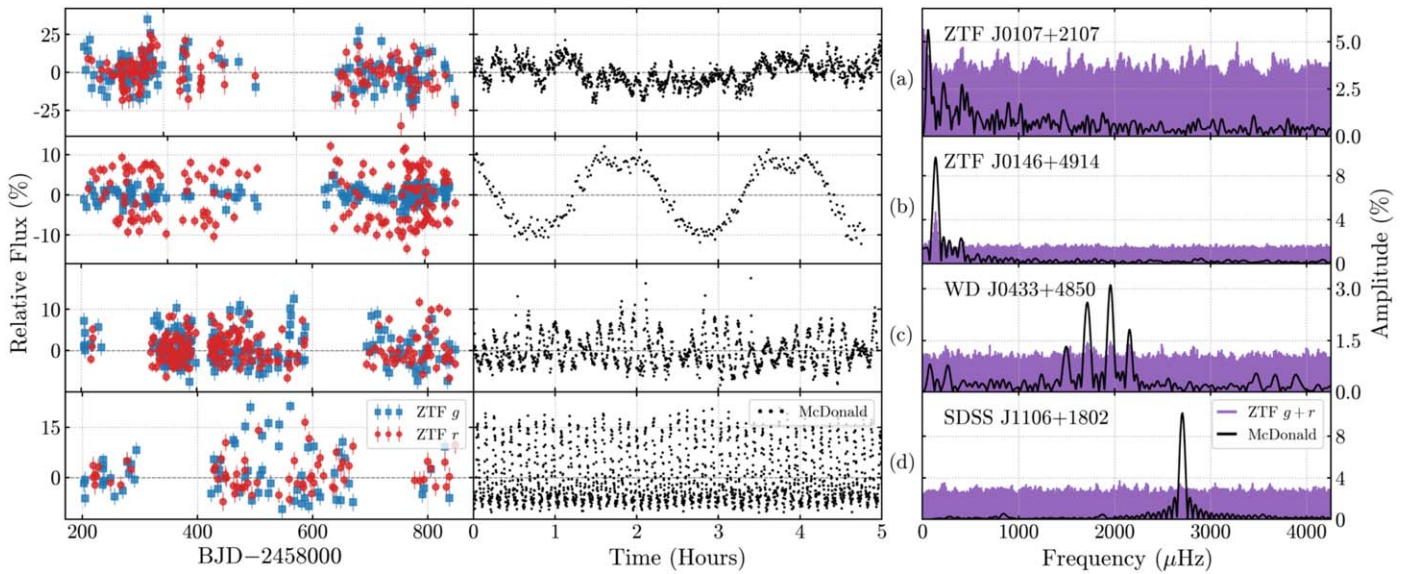


Figure 4. Four examples of new variable white dwarfs, selected from objects in our top 1% ranked list using Gaia+ZTF empirical variability. Leftmost panel shows ZTF g -band (blue squares) and r -band (red circles) photometry. Middle panel shows high-speed, follow-up photometry from McDonald Observatory. Purple periodograms at right represent the combined ZTF g - and r -band photometry. Black periodograms represent the McDonald photometry. The four objects showcased here are: (a) ZTF J0107+2107, a new transiting debris candidate; (b) ZTF J0146+4914, a new candidate polar; (c) WD J0433+4850, a known ZZ Ceti (Vincent et al. 2020); and (d) SDSS J1106+1802, a new high-mass ZZ Ceti. Notably, even with barycentric corrections applied, we do not observe significant pulsation modes in the ZTF periodograms of these two ZZ Ceti. Thus, our method is able to identify pulsating ZZ Ceti that peak-finding algorithms would otherwise neglect, while also detecting more exotic variability types like those shown in the top two panels.

their g , r , or $g+r$ periodograms above their respective thresholds. These periodicities are tabulated in Appendix G.

Since most of these periodicities we report are driven by pulsations, it should be noted that the pulsation modes in ZZ Ceti are commonly observed to vary significantly in frequency and amplitude over long-baseline observations, prompting large uncertainties from the modulations caused by this signal incoherence (see Greiss et al. 2014; Hermes et al. 2017b). This could help explain why we do not observe the pulsation modes of objects like WD J0433+4850 with the ZTF time series in Figure 4. However, for SDSS J1106+1802 and the shortest-period pulsators, it is more likely that the ZTF public survey’s typical mean sampling rate of ≈ 3 day is too long to resolve their pulsations even with hundreds of observations.

Nonetheless, this search led us to the confirmation of periodic variability in several white dwarfs we did not follow up, among which is WD J062555.04–141442.31 (ZTF J0625–1414), a previously uncataloged object that demonstrates behavior not indicative of ZZ Ceti pulsations when folded on its most significant periodicity of 4.46 hr. The remaining candidates are believed to be ZZ Ceti, given their computed periodicities and inferred placement in the Gaia CMD, and are discussed in Section 6.

Our follow-up observations at McDonald Observatory indicated the discovery of six new objects that have temperatures far from the ZZ Ceti instability strip that also demonstrate variability not indicative of pulsations. These observations are shown in Appendix C, under the panel dedicated to non-ZZ Ceti. Because our follow-up is limited, however, we could not definitively constrain the detected variability for one object with our photometry alone. WD J053432.93+770757.40 (ZTF J0534+7707), a new nonpulsating white dwarf, exhibits 0.72 hr variability that appears to resemble the rotation of a dark spot on the surface of a magnetic white dwarf, e.g., SDSS J1529+2928 (Kilic et al. 2015). Follow-up spectroscopy to search for Zeeman

splitting could confirm this classification, but is outside the scope of our work here.

Another nonpulsating white dwarf we discovered is WD J014635.73+491443.10 (ZTF J0146+4914), which exhibits peak-to-peak variations of $\approx 20\%$ in the r band in its ZTF and McDonald photometry (Figure 4), while its ZTF g -band photometry shows no evidence for variability. Only when analyzing the multicolor photometry obtained using the McDonald 2.1 m telescope through the SDSS- g/r filters, phase-folded on a period of 2.057 hr, do more subtle variations of 2.5% amplitude emerge in the g band.

We show in Figure 5 time-resolved LRS2-B spectroscopy, with each spectrum labeled by the phase at mid-exposure. The strong cyclotron emission features, which vary in strength with phase, suggest that this object is a highly magnetic polar. The two features (at ≈ 6000 Å and ≈ 4000 Å) could correspond to the second and third harmonics, respectively, of cyclotron emission due to a magnetic field of $B \approx 89$ MG (Ferrario et al. 1996). Assuming the 2.057 hr signal is the orbital period, this object falls slightly below the orbital period gap observed for cataclysmic variables (CVs) and lies in the middle of the distribution for magnetic CV systems (Witham et al. 2006). Furthermore, its distance of 56.3 ± 0.3 pc (Bailer-Jones et al. 2018) could potentially establish ZTF J0146+4914 as the closest known polar to date (Belloni et al. 2020; Pala et al. 2020).

Inspecting the magnitude distributions of our top 1% sample, we find that our Gaia+ZTF method appears robust down to roughly $G < 18.5$ mag, whereas the Gaia-only method is sufficient to $G < 20.0$ mag. Our sensitivity to variability, defined as the relative fraction of objects in the top 1% at a given magnitude, decays quickly when we go fainter than $G \approx 18.5$. Beyond this limit, we detect two known variable white dwarfs, WD J153615.98–083907.53, a CV with $G = 18.9$ mag, and WD J013906.17+524536.89 (ZTF J0139+5245), one of the two known white dwarfs with transiting planetary

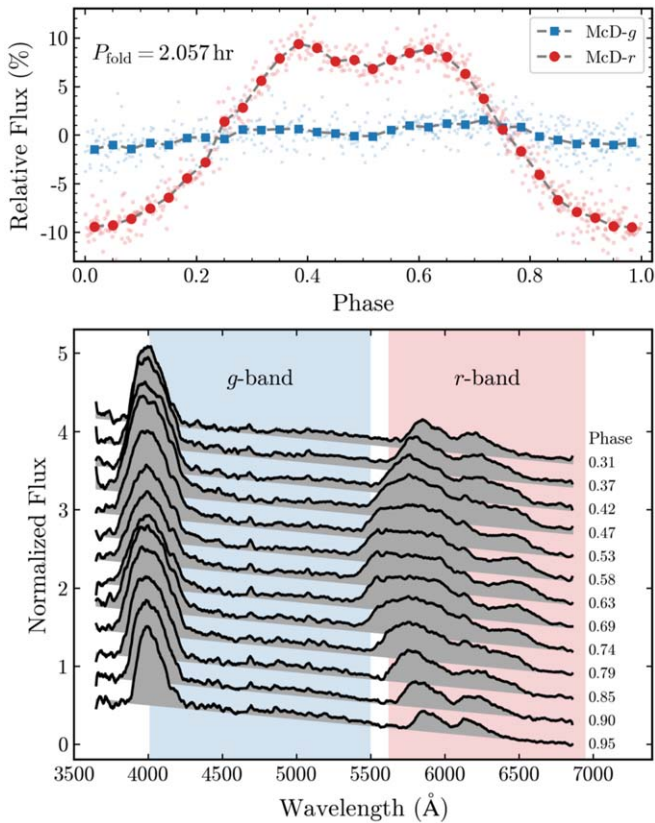


Figure 5. Top: phase-folded McDonald 2.1 m *g*- and *r*-band photometry of a new polar found from our variability metric, ZTF J0146+4914, folded at a period of 2.057 hr. Bottom: time-resolved HET LRS2-B spectroscopy of ZTF J0146+4914, each labeled by the phase at mid-exposure, showing cyclotron emission features varying in strength with phase. The features at ≈ 6000 Å and ≈ 4000 Å could correspond to the second and third harmonics, respectively, of cyclotron emission due to a magnetic field of $B \approx 89$ MG. Colored regions show the extents of the *g* and *r* filters, while gray shading under each spectrum is used to accentuate the changing strength of the cyclotron emission.

debris with $G = 18.5$ mag. These fainter objects exhibit very high amplitude variability, exceeding 30% in peak-to-peak amplitude. Therefore, it stands to reason that this is a requirement for objects fainter than $G \approx 18.5$ to be detected by our Gaia-ZTF method, especially given that the associated random noise in the flux measurements of an object grows with magnitude. For the same reason, these objects must manifest larger brightness variations to trigger ZTF alerts, which is also responsible for the dearth of candidates at fainter magnitudes relative to the Gaia-only technique.

5. White Dwarfs with Transiting Debris

Among the top 1% most variable Gaia-ZTF white dwarfs are WD J114833.63+012859.42 (WD 1145+017; Vanderburg et al. 2015) and WD J013906.17+524536.89 (ZTF J0139+5245; Vanderbosch et al. 2020), the only two previously known white dwarfs with transiting planetary debris. Accompanying these detections are four additional objects within the top 1% that exhibit transit-like dips in their ZTF light curves or McDonald 2.1 m follow-up photometry, shown in Figure 6. An additional object ranked in the top 1% from our Gaia-only method also appears to have transit-like dips on short timescales in its McDonald 2.1 m photometry, and is known to show metal pollution in previous spectroscopic studies. If all five candidates

are confirmed, this would more than triple the number of known white dwarfs hosting transiting planetary debris, while also increasing the diversity of observed transit durations and recurrence timescales. The light curves of these seven objects are displayed in Figure 6, organized by transit timescales.

ZTF J092311.41+423634.16 (ZTF J0923+4236), the fifth-most variable white dwarf within 200 pc according to our Gaia-ZTF ranking parameter, demonstrates multiple transit-like phenomena of varying durations and depths. The highest-resolved of these features at MJD ≈ 58450 closely resembles a mirror image of the dips observed for ZTF J0139+5245 (Vanderbosch et al. 2020): this object displays a gradual ingress and sharp egress, also contrasting the transit shapes of WD 1145+017 (Figure 6) and the K dwarf KIC 12557548 (Rappaport et al. 2012; van Lieshout et al. 2016). Unlike those in ZTF J0139+5245, the observed transits in ZTF J0923+4236 appear more incongruous and complex, repeating on irregular intervals with varying shapes. The dip at MJD ≈ 58450 appears to have a secondary feature before the onset of the larger dip. This more complicated structure, which appears to be transiting on the order of days, implies ZTF J0923+4236 may be at an evolutionary stage in between WD 1145+017 (roughly 4.5 hr orbital period) and ZTF J0139+5245 (roughly 107 day orbital period). We followed up ZTF J0923+4236 with high-speed photometry on MJD = 59138 and 59139, using the McDonald 2.1 m telescope to assess short-term variability, observing small amplitude variations on timescales of ≈ 1 hr (Appendix C). These observations, however, were constrained to less than two hours in length, due to the observing conditions. McDonald 2.1 m observations on MJD = 59168 spanning 3 hr in length do not show this same possible short-term variability to within the 4 σ significance threshold (Appendix C). We observe broad Balmer lines in a relatively low-resolution follow-up spectrum from HET (see Figure 7), and classify ZTF J0923+4236 as a DA white dwarf. The lack of emission lines disfavors cataclysmic variable activity as the cause of photometric variability, leaving transiting planetary debris as a likely explanation. Future monitoring is suggested to place stronger constraints on the source of these transit-like features and any metal pollution or circumstellar gas around this white dwarf.

ZTF J034703.18+180253.49 (ZTF J0347+1802) is the other white dwarf showing likely long-term transits, observed to undergo a ≈ 70 day long flux dip in its ZTF light curve (Figure 6). Roughly 6.4 hr of high-speed McDonald photometry both during and outside the flux dip showed no short-term variability, to a limit of 0.87% (Appendix C). The months-long duration of this transit, while still poorly constrained, likely suggests this object has a very long orbital period. ZTF J0347+1802 may be unique among these systems by offering a window into the early stages of tidal shredding of a rocky body. Serendipitously, our McDonald follow-up observations were obtained on MJD = 58727 and 58728, placing them near the deepest portion of the ZTF transit. The calibrated apparent magnitudes from these observations agree with those of ZTF, confirming that the white dwarf got dimmer during this event. We do observe broad hydrogen absorption features in relatively low-resolution follow-up spectroscopy from LDT without any obvious metal pollution (Figure 7), and classify ZTF J0347+1802 as a DA white dwarf.

SDSS J010749.38+210745.84 (SDSS J0107+2107) is a metal-polluted DAZ white dwarf with existing SDSS spectra (Kepler et al. 2015) also in our top 1%. In its ZTF photometry,

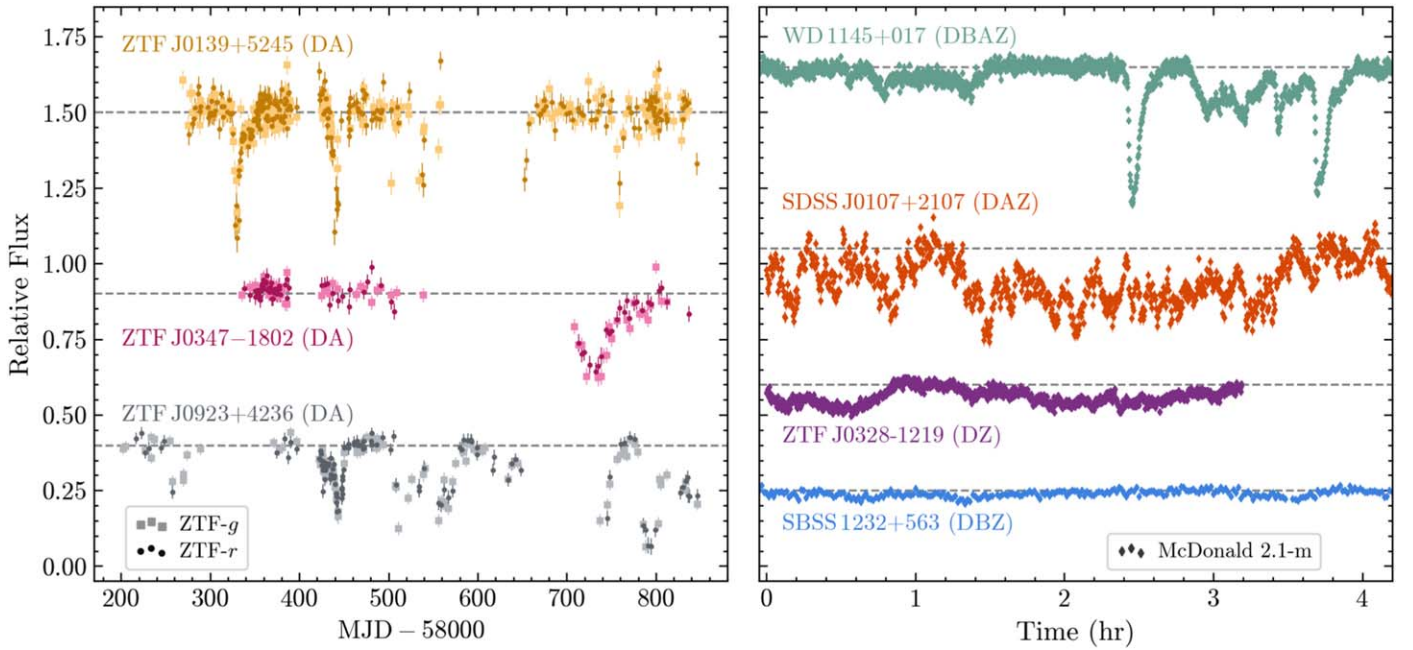


Figure 6. Left: ZTF DR3 light curves for the second known transiting debris host, ZTF J0139+5245 (top), along with two transit candidates exhibiting irregularly shaped flux dips on days-long timescales (ZTF J0347-1802 and ZTF J0923+4236). Light curves have been vertically shifted for clarity. Spectral types are shown in parentheses next to each object’s name, with references in Table 3. Right: McDonald 2.1 m high-speed photometry for the first known transiting debris host, WD 1145+017 (top), along with three more transit candidates (SDSS J0107+2107, ZTF J0328-1219, and SBSS 1232+563) that exhibit flux dips on much shorter timescales, from minutes to hours. None of these objects are cataclysmic variables, as none show spectroscopic evidence of high accretion rates via emission features (see also Figure 7).

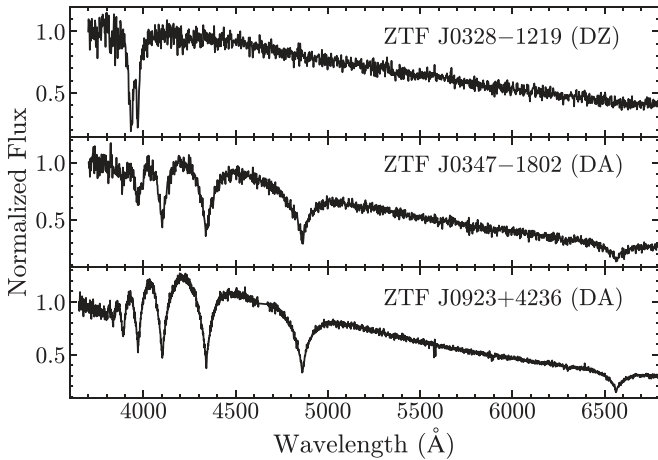


Figure 7. Follow-up identification spectra from LDT and HET of the new transiting debris systems without previous spectroscopy: ZTF J0328-1219 (top, DZ), ZTF J0347-1802 (middle, DA), and ZTF J0923+4236 (bottom, DA). While ZTF J0328-1219 is the only one to show strong evidence of metal pollution via the prominent Ca II H & K lines, additional spectroscopic follow-up at higher signal-to-noise is warranted for ZTF J0347-1802 and ZTF J0923+4236, as the strength of Ca features may be correlated with transit depth if due to circumstellar absorption (Vanderbosch et al. 2020).

SDSS J0107+2107 continuously exhibits large amplitude scatter (Figure 4). The high-speed photometry we obtained from McDonald corroborates this scatter, revealing essentially continuous transits, many with depths exceeding 25% in our blue, broad-bandpass *BG40* filter. This would make SDSS J0107+2107 the coolest white dwarf to exhibit planetary debris transits, with an effective temperature below 8400 K (see Table 3).

ZTF J032833.52-121945.27 (ZTF J0328-1219) also reveals essentially continuous transits in its McDonald photometry. Similar to SDSS J0107+2107, this object is cool and likely

underluminous in the Gaia color-magnitude diagram compared to most $0.6 M_{\odot}$ white dwarfs. The short-term variations in the photometry of this object are substantially shallower than those of SDSS J0107+2107 and WD 1145+017. Identification spectroscopy obtained using LDT (see Figure 7) shows deep absorption from the Ca II H & K lines, and we classify this as a DZ white dwarf.

WD J123432.68+560643.03 (SBSS 1232+563) is our least dramatic candidate for transiting debris, but it is worth brief mention. Although this object did not rank among the top 1% most variable white dwarfs with the combined Gaia-ZTF method, it was in the top 1% using the Gaia-only metric, as it had $\text{VARINDEX} = 0.025$. We followed this star up with more than 36 hr of high-speed photometry from McDonald Observatory, one night of which is shown in Figure 6. This follow-up revealed shallow, transit-like dips on relatively short timescales. Previous spectroscopy from the SDSS Digital Sky Survey has shown SBSS 1232+563 to be a metal-polluted white dwarf (Kleinman et al. 2013), indicating the presence of rocky debris in the circumstellar environment.

The three systems that appear to undergo transits on short timescales are optimal candidates to follow up with multi-epoch spectroscopy, especially short-cadence spectrophotometry to probe for substructures within the transiting debris, as previously done for WD 1145+017 (Izquierdo et al. 2018). Extended photometric campaigns of these systems are also encouraged to search for repeating patterns and variations in transit shapes, which have been observed to vary subtly on orbit-to-orbit timescales but more dramatically on longer timescales around WD 1145+017 (Gänsicke et al. 2016; Rappaport et al. 2016, 2018).

Based on the irregular and varied timescales, we show in Figure 8 that the known and candidate transiting debris systems often stand out when comparing different variability metrics,

Table 3
Table of Parameters for the Known and New Candidate White Dwarfs with Transiting Planetary Debris

Object	α (deg)	δ (deg)	d (pc) (1)	G	T_{eff} (K)	$M_{*,\text{phot}}$ (M_{\odot})	$M_{*,\text{spec}}$ (M_{\odot})	Spectral Type
Known White Dwarfs with Transiting Debris								
ZTF J0139+5245	24.77633	52.76027	$172.9^{+7.7}_{-7.2}$	18.5	9420 ± 580	0.52 ± 0.11	0.52 ± 0.03 (2)	DA (2)
WD 1145+017	177.13994	1.48316	$141.2^{+2.5}_{-2.5}$	17.2	$15,080 \pm 640$	0.64 ± 0.06	†	DBZ (3)
New Candidate White Dwarfs with Transiting Debris								
SDSS J0107+2107	16.95550	21.12910	$90.2^{+3.9}_{-3.5}$	19.2	7590 ± 800	1.08 ± 0.13	0.43 ± 0.03 (4)	DAZ (5)
ZTF J0328–1219	52.14013	–12.32930	$43.3^{+0.2}_{-0.2}$	16.6	8550 ± 160	0.86 ± 0.03	...	DZ (6)
ZTF J0347–1802	56.76399	–18.04825	$76.4^{+0.8}_{-0.7}$	17.4	$13,370 \pm 510$	1.13 ± 0.02	...	DA (6)
ZTF J0923+4236	140.79749	42.60934	$147.2^{+2.8}_{-2.7}$	17.5	$13,110 \pm 420$	0.62 ± 0.03	...	DA (5)
SBSS 1232+563	188.63559	56.11195	$173.0^{+3.7}_{-3.5}$	18.1	$11,670 \pm 600$	0.58 ± 0.07	†	DBAZ (7)

Note. All parameters are sourced from the Gentile Fusillo et al. (2019) catalog unless otherwise specified below, with α and δ being from the J2015.5 epoch. (1) Bailer-Jones et al. (2018), (2) Vanderbosch et al. (2020), (3) Vanderburg et al. (2015), (4) Kepler et al. (2019), (5) Kepler et al. (2015), (6) This work (see Figure 7), (7) Kleinman et al. (2013) †—For these objects, spectroscopic $\log(g)$ and mass estimates are highly uncertain due to modeling difficulties of helium absorption lines with metal pollution.

especially comparing the ZTF point-to-point scatter metric to the ZTF standard deviation metric. Additionally, the transiting systems occasionally stand out when comparing the final ZTF variability metric to the Gaia variability metric. This may result from cases where the Gaia photometry is more aggressively sigma-clipped than the ZTF photometry. Detailed follow-up of objects that stand out in Figure 8 may also make the search for new transiting white dwarfs more efficient. The individual ZTF images of these objects in discrepant regimes, e.g., $\tilde{V}_{\text{ZTF}} \gg \tilde{V}_G$, should also be carefully inspected by hand to ensure the discrepancy is not due to artifacts producing false scatter, such as optical ghosts, nearby bright stars, or bad pixel columns.

We conclude by noting one other possible signature to make searches for transiting white dwarfs more efficient: an appearance of being underluminous in the Gaia color–magnitude diagram, possibly due to excess circumstellar extinction resulting in erroneous photometric $\log(g)$ inferences. It is noteworthy from Table 3 that at least three of our new systems have photometrically determined T_{eff} and $\log(g)$, and thus their overall masses are much larger than the mean mass of field white dwarfs, i.e., roughly $0.6 M_{\odot}$ (e.g., Tremblay et al. 2016). It may be especially efficient to search for new transiting systems in cases where a star shows both large photometric scatter as well as discrepant spectroscopic and photometric masses, where both are known for a given white dwarf.

Our use of variability metrics from Gaia DR2 and ZTF has potentially more than tripled the number of white dwarfs that are known to be transited by planetary debris, but we emphasize that we have restricted our search in distance (<200 pc) and to photometric temperatures near the ZZ Ceti instability strip. There is great potential in searching more broadly for white dwarfs with transiting planetary debris using these techniques. We believe that, because our standard deviation metric dominates on timescales when the variability periods are much greater than the sampling rate, future targeted applications of this method extended to all white dwarf temperatures and a larger space volume should yield an even larger increase in new candidate transiting debris systems.

6. New Confirmed ZZ Cetis

We report the confirmation of 29 new ZZ Ceti using follow-up high-speed photometry: 9 of these were discovered from our

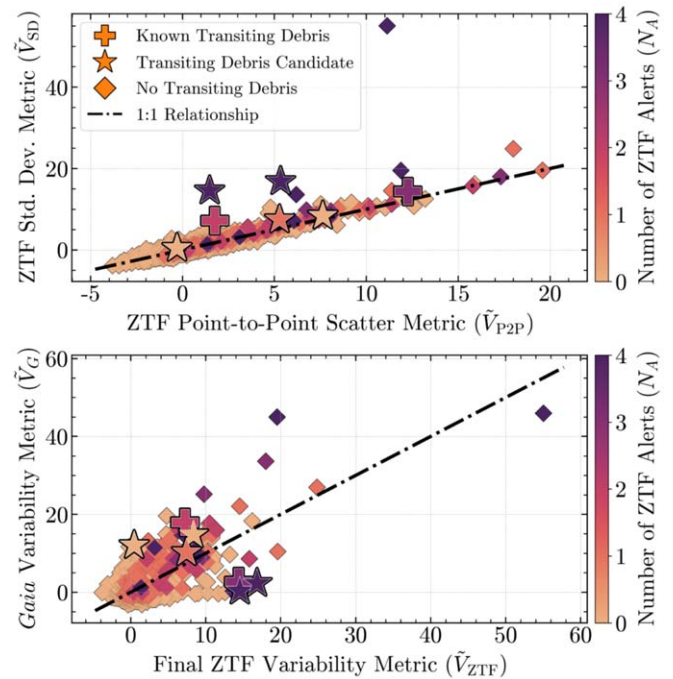


Figure 8. Top: comparison between the detrended ZTF light-curve standard deviation metric (\tilde{V}_{SD}) against the point-to-point scatter metric (\tilde{V}_{P2P}). There is generally 1:1 agreement between the two metrics, except for the handful of objects whose longer-term variability dominates, e.g., transits from planetary debris. Objects are color-coded by their ZTF alert metric value, N_A . Bottom: comparison between the Gaia metric (\tilde{V}_G) vs. the finalized ZTF metric (\tilde{V}_{ZTF}). Regions deviating from the 1:1 agreement are particularly rich areas of interest, as evidenced by the detection of two transiting planetary debris system candidates in the $\tilde{V}_{\text{ZTF}} \gg \tilde{V}_G$ regime.

Gaia-only metric described in Section 3.1, and the other 20 were discovered from our Gaia-ZTF metrics described in Section 3.2. This marks our study as the second to use Gaia DR2 to discover a substantial amount of new ZZ Cetis, following the results of Vincent et al. (2020). Unlike the Vincent et al. (2020) study, we did not conduct a targeted search of ZZ Cetis—rather, we fixated our search on the ZZ Ceti instability strip, to use the detection of ZZ Ceti as a proof of concept. We also report the identification of eight more new ZZ Cetis using their ZTF time series, as well

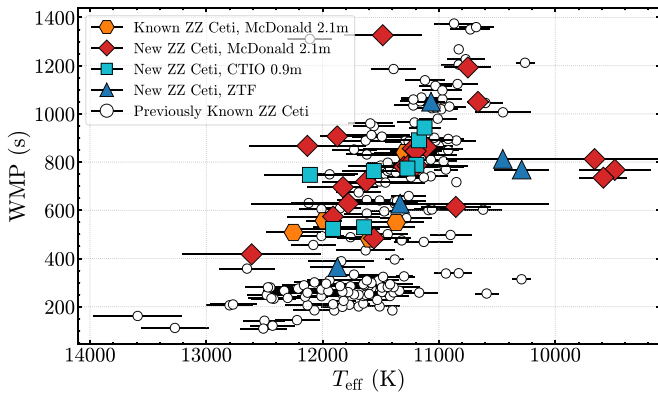


Figure 9. Distribution of weighted mean pulsation periods (WMP) for independent, significant peaks as a function of photometrically determined effective temperature (Gentile Fusillo et al. 2019). White circles mark previously analyzed ZZ Ceti (Mukadam et al. 2006; Hermes et al. 2017b), while red diamonds and cyan squares indicate new ZZ Ceti found using this method with follow-up photometry from the McDonald 2.1 m and CTIO 0.9 m, respectively. We show the six known ZZ Ceti from the Vincent et al. (2020) study we observed as orange hexagons, and the seven new ZZ Ceti that show significant periods in their ZTF light curves as blue triangles. As pulsating white dwarfs cool, their convection zones deepen, driving characteristically longer-period and higher-amplitude pulsations (e.g., Clemens 1993). Our variability metrics thus preferentially discover cooler pulsating white dwarfs with longer pulsation periods.

as their inferred placement in the ZZ Ceti instability strip using Gaia DR2 color information.

Since our methods prioritize objects with the most anomalous levels of scatter, most of these new pulsating white dwarfs are characterized by high-amplitude pulsations at long periods. This bias is best demonstrated in Figure 9, where the weighted mean pulsation periods (WMP) are plotted against T_{eff} . WMP is calculated for a given white dwarf from its linearly independent pulsation period(s), P , and corresponding amplitude(s), A , using the relationship: $\text{WMP} = (\sum_i P_i A_i) / (\sum_i A_i)$.

The significant pulsation modes for each ZZ Ceti were determined using the Python package PYRIOD (Bell 2020)²¹ to conduct a prewhitening routine by hand. We compute the Lomb–Scargle periodogram of each object’s McDonald or CTIO time series, and then subtract peaks surpassing the standard $4\langle A \rangle$ significance threshold until no significant peaks remain in the residual periodogram. We found and removed any combination and harmonic frequencies among the significant peaks to within a frequency tolerance of 0.5 divided by the length of the light curve in seconds, in order to determine all the linearly independent, significant pulsation modes present for each object. Only peaks corresponding to periods $80 < P < 2000$ s were considered, as these bounds form the approximate range for adiabatic nonradial g -mode pulsations in ZZ Ceti (Romero et al. 2012). These pulsation spectra are fully detailed in Appendix G.

Our distribution of WMP in Figure 9 reveals that our method is biased toward finding the highest-amplitude pulsating white dwarfs, which tend to occur in the coolest pulsators with the longest-period pulsation modes. This trend has been noted before in ensemble studies of ZZ Ceti, notably in Clemens (1993) and Mukadam et al. (2006). A more complete search for more pulsating white dwarfs across the entire ZZ Ceti instability strip may require relaxing the threshold that the object must be among the 1% most variable of all white dwarfs,

but would return a more representative distribution, like the one attained by Vincent et al. (2020).

Notably, we did not discover pulsations in any new extremely low-mass (ELM, $< 0.3 M_{\odot}$) white dwarfs in our Gaia+ZTF sample. This is likely because our temperature selection required targets to have photometrically determined temperatures and surface gravities in Gentile Fusillo et al. (2019), and most ELM white dwarfs do not have values in their DR2 catalog. The space density of ELM white dwarfs is also relatively low, so there are also few within 200 pc (Kawka et al. 2020). However, we demonstrate that pulsations in ELM white dwarfs can be found from variability metrics using our Gaia-only sample: WD J184424.33+504727.95 ($G=17.9$ mag) is a new pulsating ELM white dwarf confirmed to exhibit long-period pulsations from McDonald Observatory (Appendix C) consistent with known ELM pulsation periods (Hermes et al. 2013). We exclude this likely He-core white dwarf from Figure 9, but its dominant pulsation period is 4220 s and its WMP exceeds 3900 s.

Using these variability metrics may also prove fruitful in improving our understanding of the high-mass regime of the ZZ Ceti instability strip, as we discovered three new ZZ Ceti with $\log(g) > 8.5$. Most notably, WD J110604.54+180233.72 (SDSS J1106+1802), the most massive of these, has an inferred photometric surface gravity of $\log(g)=8.8$ (Gentile Fusillo et al. 2019), whereas fits to its SDSS spectra imply $\log(g)=9.04 \pm 0.03$ (Kepler et al. 2015). We show in Figure 4 and Appendix C that this object undergoes stable, high-amplitude pulsations of order 25% in peak-to-peak amplitude at a period of 369.7 s. The amplitude of these pulsations is particularly notable, given that higher-mass white dwarfs have smaller resonant cavities relative to average-mass pulsating white dwarfs, and thus are expected to demonstrate lower-amplitude pulsations (Castanheira et al. 2010). Further spectroscopy of this target may also help define the high-mass blue edge of the ZZ Ceti instability strip: while its photometric temperature is $T_{\text{eff}}=12610$ K (Gentile Fusillo et al. 2019), its spectroscopic temperature is $T_{\text{eff}}=14220 \pm 110$ K (Kepler et al. 2015).

Our methods can also reveal other exotic pulsating white dwarfs. Since ZTF is optimized to trigger alerts for transient phenomena, our methods may also be used to detect outbursts from ZZ Ceti in the future. Outbursts were first seen using continuous monitoring from the Kepler space telescope, and appear to be an internal effect in the coolest pulsating white dwarfs, causing them to undergo a mean flux increase of at least 15%, with durations on the order of hours (Bell et al. 2015, 2016; Hermes et al. 2015). At least two of our newly confirmed ZZ Ceti, WD J203737.79+323833.34 and WD J060102.01+541757.82, were observed to increase in relative flux by factors of order $\gtrsim 20\%$ on multiple occasions by ZTF. ZTF also observed WD J032438.66+602055.88 to undergo numerous sporadic flux increases exceeding 12%, which is at least a factor of two increase in amplitude relative to its largest pulsation amplitudes observed from McDonald Observatory. These flux increases could be simply explained by the beating of pulsation modes, though. Still, given the presence of long-period pulsation modes in their follow-up periodograms from McDonald Observatory, these three objects should be closely monitored in the event they undergo future outbursts.

²¹ <https://github.com/keatonb/Pyriod>

The transient identification capabilities of ZTF also shed light on WD J191852.42+583914.09 (ZTF J1918+5839), a newly discovered low-amplitude pulsator confirmed with McDonald photometry, was observed to undergo an enormous flux increase of order $\approx 150\%$, slowly decaying over the course of about 10 days in its ZTF DR3 photometry. This would vastly exceed the amplitude and duration of any previously observed outburst in a pulsating white dwarf. The *J*-band photometry from the United Kingdom Infra-Red Telescope (UKIRT) Hemisphere Survey (UHS; Dye et al. 2018) is consistent with an isolated white dwarf model. Deeper near-infrared imaging could help us rule out a cool line-of-sight companion, since ultracool dwarfs can undergo massive ($\Delta V \sim -10$ mag) flares (e.g., Jackman et al. 2019).

Two additional objects in our top 1% demonstrated similar phenomena. WD J144823.77+572454.62 (ZTF J1448+5724) was observed by ZTF to undergo a relative flux increase of $>80\%$ in *g* that decayed back to its median flux over the course of two days. WD J134934.36+280948.93 (ZTF J1349+2809) was observed by ZTF to nonmonotonically increase from approximately 20% to over 85% during six *g*-band observations over the course of about 1.94 hr. Archived optical photometry and WISE W1 and W2 photometry of ZTF J13349+2809 are consistent with the Koester (2010) DA white dwarf model at the inferred $T_{\text{eff}} = 11,250$ K and $\log(g) = 8.0$ from Gentile Fusillo et al. (2019). While ZTF J1448+5724 does not possess WISE benchmarks, its SED is consistent with the Koester isolated DA white dwarf model at its inferred $T_{\text{eff}} = 10,750$ K and $\log(g) = 7.75$ (Gentile Fusillo et al. 2019). Notably, both objects have atmospheric parameters (assuming a DA composition) that place them in a parameter space where ZZ Ceti have been observed to undergo outbursts (Hermes et al. 2017b).

Finally, within the top 1% sample, we identify eight more new ZZ Ceti using the ZTF time series alone. Seven of these objects were identified after observing significant frequencies in their Lomb–Scargle periodograms beyond their estimated 0.1% false alarm probability significance thresholds at frequencies greater than $500 \mu\text{ Hz}$. For three of these objects, WD J062516.34+145558.50, WD J143047.25+510730.35, and WD J233921.05+512410.79, these detections were aided by multiple nights of dense short-cadence observations that resolved consecutive pulsation peaks. Likewise, despite not showing any significant periodicities, WD J182454.39+344331.58 was also densely imaged at short cadence during two nights in the *r*-band, which resolved variability indicative of ZZ Ceti pulsations. All eight objects have a position in the Gaia CMD within the ZZ Ceti instability strip, further warranting their classification.

7. Conclusions

We have established a novel method capable of identifying variable white dwarfs of numerous types up to $G \approx 19$ mag using excess levels of scatter in Gaia DR2 and ZTF DR3 photometry and ZTF alerts. We applied the metrics to a population of about 12,100 known and candidate white dwarfs within 200 pc and with temperatures near the ZZ Ceti instability strip, analyzing the top 1% most variable objects. We have fully demonstrated our method with complimentary high-speed photometry from the 2.1 m Otto Struve telescope at McDonald Observatory, confirming variability in all 33 out of 33 objects we observed in the top 1%, i.e., a 100% success rate. We also present an easily reproducible global Gaia-only metric

valid over $13 \lesssim G \lesssim 20$ for DR2 photometry. We followed up eight white dwarfs with the Cerro Tololo Inter-American Observatory SMARTS 0.9 m telescope identified as variable candidates with this technique, confirming ZZ Ceti pulsations in all eight.

Among the previously known and newly confirmed variable white dwarfs we found are mostly pulsating white dwarfs, along with smaller numbers of cataclysmic variables, eclipsing binaries, and transiting debris systems. Our methods recover the only two previously known white dwarfs to show planetary debris transits, and we detect five new candidate transiting debris systems. Given that our target selection was restricted in temperature and distance, we expect to detect many more white dwarfs hosting transiting planetary debris in future applications to forthcoming Gaia and ZTF data releases, turning these objects into a class we can study to look for differences in debris evolution and dynamics.

While our methods are demonstrated and highly efficient, we acknowledge that they are limited in scope, as we cannot yet confidently classify or identify variability based on excess levels of scatter alone. Follow-up time-series and spectroscopic observations are essential to tapping the full potential of this technique in order to fully characterize the true nature of these objects and systems. We expect that ongoing and upcoming all-sky surveys, and their commitment to public data releases, will provide the community many new exciting variable white dwarfs for years to come.

We thank the anonymous referee for reviewing the manuscript and providing helpful comments. We also recognize Thomas Kupfer for a fruitful discussion on the Zwicky Transient Facility Galactic Plane Survey, which provided the necessary short-cadence observations for some of our detections of new ZZ Ceti using ZTF.

J.A.G. extends gratitude to the Department of Astronomy at the University of Texas at Austin for their awarding of the Summer Undergraduate Research Fellowship that supported this analysis. J.A.G. also acknowledges the Freshman Research Initiative White Dwarf Stream for all the guidance and mentoring it has provided and the doors it has opened.

Z.P.V., D.E.W., and M.H.M. acknowledge support from the United States Department of Energy under grant DE-SC0010623, the National Science Foundation under grant AST-1707419, and the Wootton Center for Astrophysical Plasma Properties under the United States Department of Energy collaborative agreement DE-NA0003843. J.J.H. and I.D.L. acknowledge ground-based observing support through the TESS Guest Investigator Program Grant 80NSSC19K0378, as well as the K2 Guest Observer program 80NSSC19K0162. B.N.B. and K.A.C. acknowledge funding through the TESS Guest Investigator Program Grant 80NSSC19K1720 and the National Science Foundation under grant AST-1812874. B.N.B. also acknowledges support from the High Point University Student Government Association, which kindly funded the observing run to the SMARTS 0.9 m at CTIO through bill #S-18-48. K.J.B. is supported by the National Science Foundation under Award AST-1903828. M.H.M. acknowledges support from the NASA ADAP program under grant 80NSSC20K0455. T.M.H. acknowledges support from the National Science Foundation under grant AST-1908119.

Follow-up observations obtained using 2.1 m Otto Struve Telescope and Hobby–Eberly Telescope at The McDonald Observatory of The University of Texas at Austin were vital for

this work. This work makes extensive use of publicly archived observations from the Zwicky Transient Facility survey, conducted with the Samuel Oschin 48 inch Telescope at Palomar Observatory. ZTF is a collaboration supported by a consortium of 12 institutions and NSF grant No. AST-1440341. We also employed data retrieved and processed the European Space Agency (ESA) Gaia mission (<https://www.cosmos.esa.int/gaia>). All Gaia data processing was orchestrated by the Gaia Data Processing and Analysis Consortium (DPAC, <https://www.cosmos.esa.int/web/gaia/dpac/consortium>). We queried observations from the Pan-STARRS1 Surveys (PS1) and the PS1 public science archive, which is supported by the consortium of 14 institutions that make up the PS1 collaboration (<https://panstarrs.stsci.edu/>) and the NSF grant No. AST-1238877. These results made use of the Lowell Discovery Telescope at Lowell Observatory. Lowell is a private, nonprofit institution dedicated to astrophysical research and public appreciation of astronomy, and operates the LDT in partnership with Boston University, the University of Maryland, the University of Toledo, Northern Arizona University, and Yale University. Finally, this research made use of data from the SMARTS 0.9 m telescope at Cerro Tololo Inter-American Observatory, which is operated as part of the SMARTS Consortium.

Facilities: PO:1.2 m (ZTF), Gaia, McD:Struve (ProEM), McD:HET (LRS2), CTIO:0.9 m, DCT (DeVeny), ADS, CDS.

Software: ASTROPY (Astropy Collaboration et al. 2013, 2018), IRAF (National Optical Astronomy Observatories), LMFIT (Newville et al. 2014), MATPLOTLIB (Hunter 2007), NUMPY (Harris et al. 2020) PANDAS (pandas development team 2020), PHOT2LC (<https://github.com/zvanderbosch/phot2lc>), PHOTUTILS (Bradley et al. 2020), PYRIOD (<https://github.com/keatonb/Pyriod>), CDS's (Strasbourg, France) SIMBAD and VizieR online pages and tables, and the NASA Astrophysics Data System (ADS) repositories.

Appendix A Gaia Astrometric Quality Cuts

Below, we show all the Astronomical Data Query Language (ADQL) astrometric quality cuts we imposed on the Gentile Fusillo et al. (2019) Gaia DR2 catalog, as recommended in Lindegren et al. (2018) and Evans et al. (2018):

VISIBILITY_PERIODS_USED > 8 & PARALLAX > 5 & PARALLAX_OVER_ERROR > 10 & ASTROMETRIC_EXCESS_NOISE < 1.0 & PHOT_PROC_MODE < 0.1 & PHOT_BP_MEAN_FLUX_OVER_ERROR > 10 & PHOT_RP_MEAN_FLUX_OVER_ERROR > 10 & PHOT_G_MEAN_FLUX_OVER_ERROR > 20 & PHOT_BP_RP_EXCESS_FACTOR < 1.3 + 0.06 * pow(PHOT_BP_MEAN_MAG - PHOT_RP_MEAN_MAG, 2) & PHOT_BP_RP_EXCESS_FACTOR

> 1.0 + 0.015 * pow(PHOT_BP_MEAN_MAG - PHOT_RP_MEAN_MAG, 2) & ASTROMETRIC_CHI2_AL / (ASTROMETRIC_N_GOOD_OBS_AL - 5) < 1.44 * maxReal (1, exp (-0.4 * (PHOT_G_MEAN_MAG - 19.5))) & (PHOT_G_MEAN_MAG + 5 * log10(PARALLAX/100)) > ((4.0 * BP_RP) + 9.0)

Appendix B Pan-STARRS Decontamination Criteria

Below, we present the decontamination criteria we imposed on our astrometrically clean sample of 18,269 objects using Pan-STARRS PS1 catalog. First, we require that objects must have real (i.e., not NAN) GMEANPSFMAG and RMEANPSFMAG values. If any of these are NANs, and the next nearest measurements are within 1''75 with $|GMEANPSFMAG - G_{BP}| \leq 0.15$ mag and $|RMEANPSFMAG - G| \leq 0.15$ mag, then those values are used for the object. Otherwise, the object is flagged and removed from the analysis.

Assuming an average FWHM seeing of 2''5 in the ZTF photometry, the remaining decontamination criteria are:

1. Objects with a neighboring star within 5''0 are flagged unless the source is at least 2.0 mag dimmer.
2. Objects with a neighboring star between 5''0 and 7''5 are flagged unless the source is at least 1.0 mag dimmer.
3. Objects with a neighboring star more than 2.0 mag brighter between 7''5 and 12''0 are flagged.
4. Objects with a 13th mag star or brighter within 30''0 are flagged.
5. Objects with a 10th mag star or brighter within 60''0 are flagged.

Appendix C McDonald 2.1 m Light Curves and Periodograms

In this appendix, we show the light curves and Lomb-Scargle periodograms from our follow-up campaign using the McDonald Observatory 2.1 m Otto Struve telescope. Figure 10 displays all six confirmed nonpulsating variables. Figure 11 shows the new ZZ Ceti we announce in this work, including the extremely low-mass pulsator WD J1844+5047 found using the Gaia-only method. Finally, Figure 12 shows our observations of the six newly announced ZZ Ceti in Vincent et al. (2020) that we followed up independently. All objects were observed through a BG40 blue-bandpass filter unless specified otherwise.

New Non-Pulsating Variables

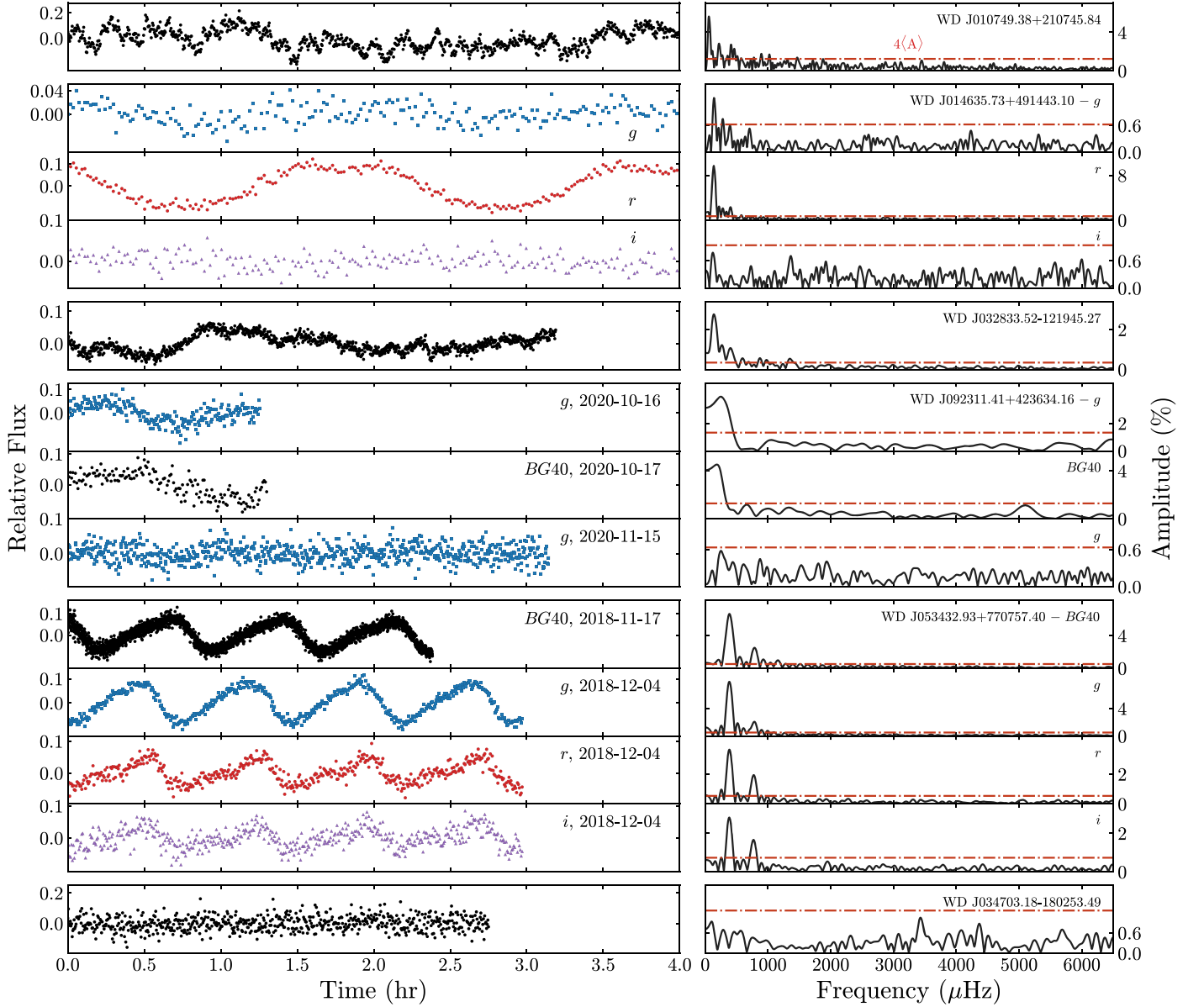


Figure 10. McDonald 2.1 m high-speed time-series photometry for the six new nonpulsating variable objects we followed up in the top 1% using Gaia+ZTF. Black dots represent observations taken in the *BG40* filter, blue squares represent SDSS *g*, red circles represent SDSS *r*, and purple triangles represent SDSS *i*. Light curves from different nights are noted. Although these photometry show ZTF J0347-1802 not to be significantly variable on short timescales, we clearly see a transit in its ZTF photometry that implies the presence of long-term variability. ZTF J0923+4236 does appear to exhibit short-term variability. Due to short observing windows at the time of observing, we are uncertain of the origin of this variability. Similarly, the origin of the consistent, stable pattern shown in the multicolor photometry of ZTF J0534+7707 is unknown, with the most likely explanation being a surface inhomogeneity such as a dark spot due to a strong magnetic field.

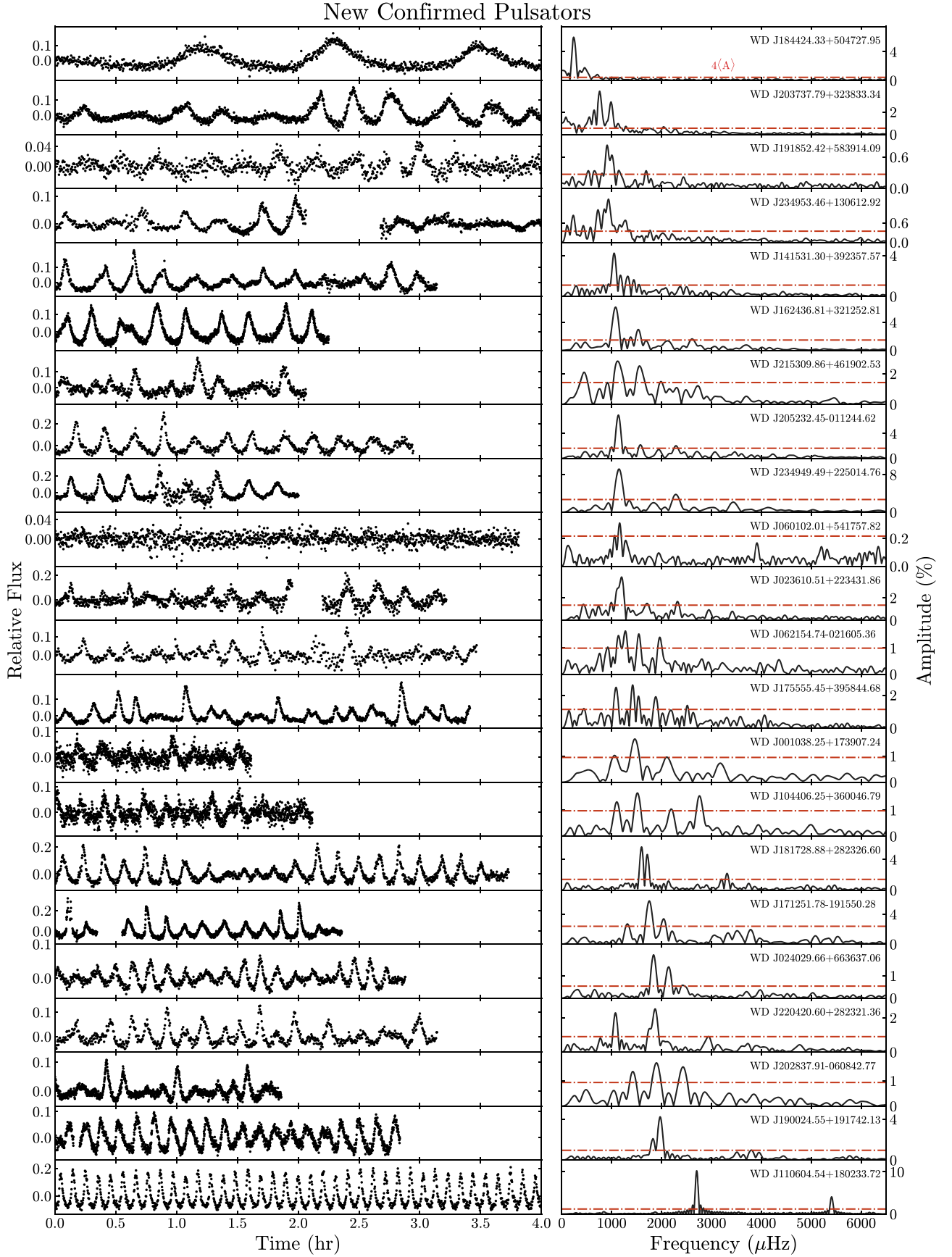


Figure 11. McDonald 2.1 m high-speed time-series photometry for the 21 new confirmed ZZ Ceti in the top 1% using Gaia+ZTF. We also show the photometry for WD J1844+5047, the new ELMV we report using the Gaia-only technique.

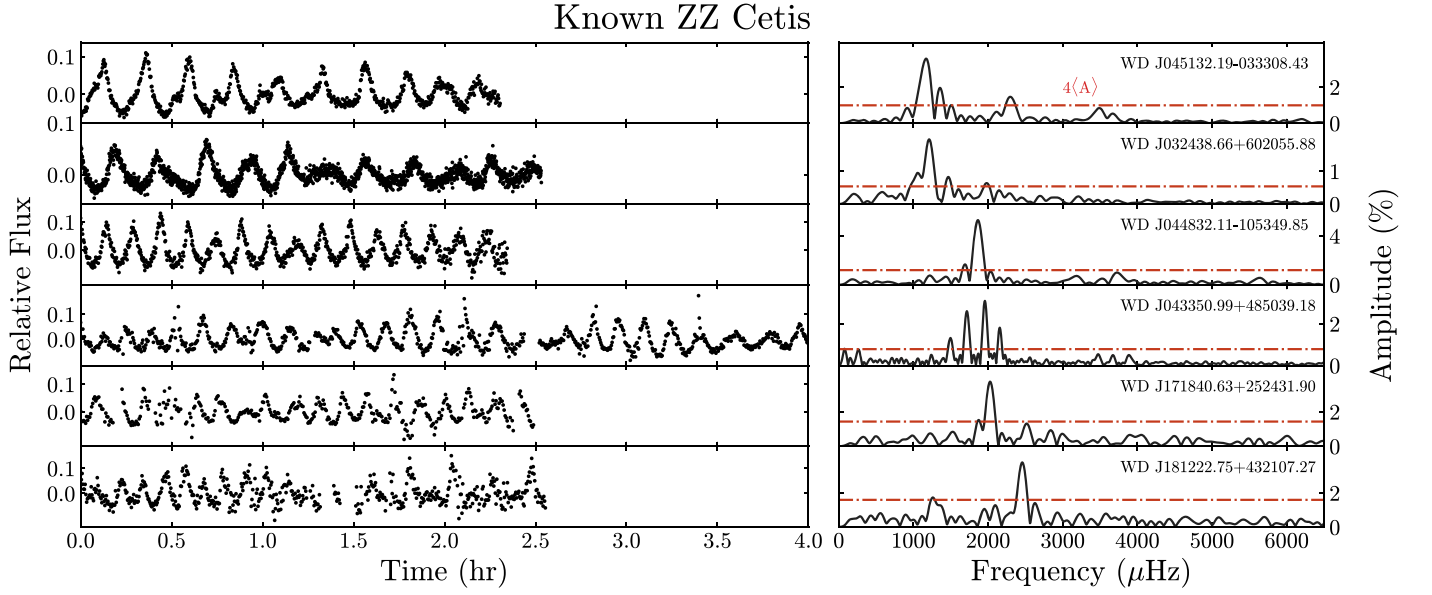


Figure 12. McDonald 2.1 m high-speed time-series photometry for six recently discovered ZZ Ceti in Vincent et al. (2020) residing in the top 1% that we independently verified.

Appendix D

CTIO SMARTS 0.9 m Light Curves and Periodograms

In this appendix, we show the light curves and Lomb–Scargle periodograms from our follow-up campaign using the SMARTS 0.9 m telescope at Cerro Tololo Inter-American Observatory.

Figure 13 shows the eight new ZZ Ceti we found using the Gaia-only method. The stellar parameters of these objects are shown in Table 4. Note that photometry of WDJ1712–1915, an object we observed at McDonald Observatory, is also shown here.

New Confirmed ZZ Ceti (CTIO)

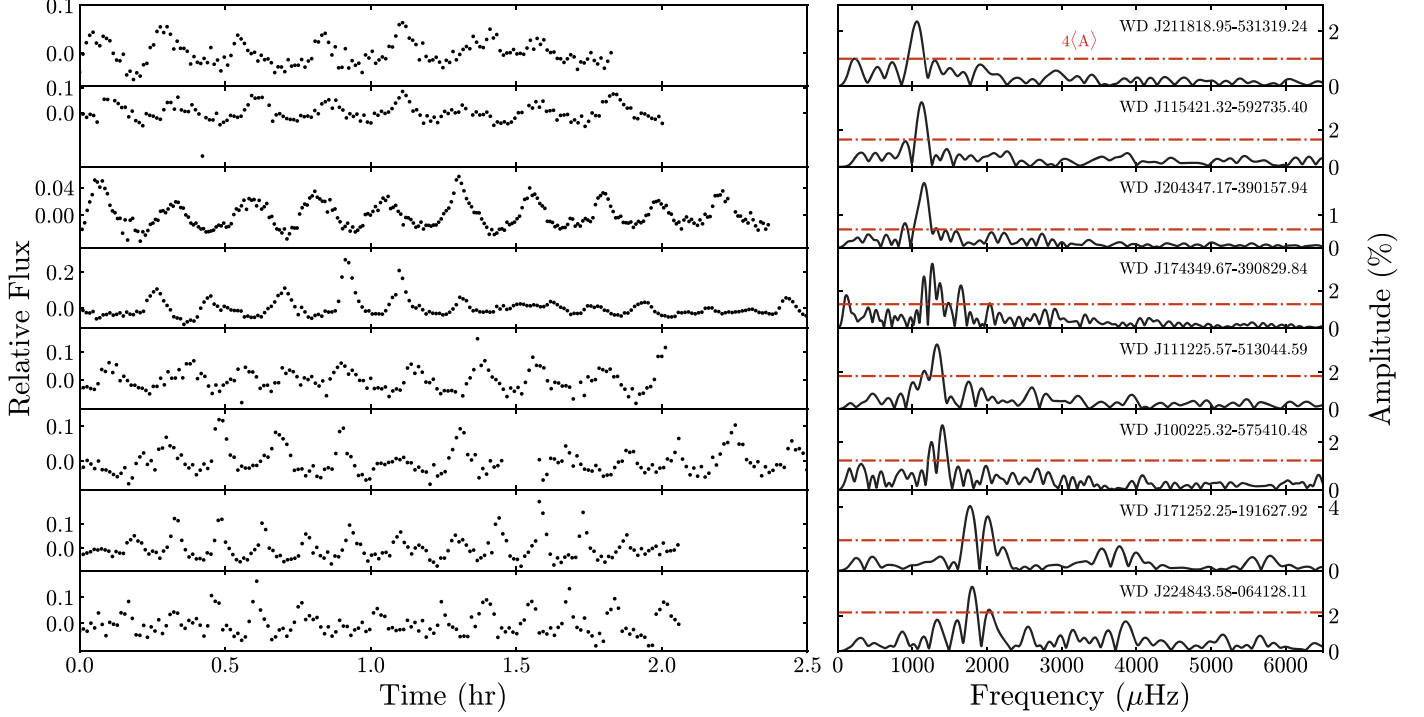


Figure 13. SMARTS CTIO 0.9 m high-speed, time-series photometry for the eight new ZZ Ceti found using the Gaia-only method.

Table 4

Table of Parameters and Metrics for New ZZ Ceti Selected from the Top 1% Most Variable White Dwarfs from Our Gaia-only Variability Search

WD	α (deg)	δ (deg)	G	T_{eff}	$\log(g)$	VARINDEX
WD J100223.96–575507.91	150.59947	–57.91868	16.8	12110	8.0	0.0130
WD J111221.43–513003.90	168.08948	–51.50112	16.4	11190	8.0	0.0121
WD J115414.55–592658.81	178.56046	–59.44960	16.9	11170	8.0	0.0100
WD J171251.78–191550.28	258.21559	–19.26396	16.3	11910	8.1	0.0261
WD J174349.28–390825.95	265.95468	–39.14034	13.6	11560	8.1	0.0246
WD J204349.21–390318.02	310.95500	–39.05652	13.8	11270	8.0	0.0063
WD J211815.52–531322.72	319.56444	–53.22334	15.9	11120	7.9	0.0086
WD J224840.07–064244.65	342.16694	–6.71254	16.9	11640	8.1	0.0257

Note. The parameters here are sourced from the Gentile Fusillo et al. (2019) catalog, with α and δ representing the J2015.5 epoch.

Appendix E

The Gaia Variability Metric as a Global Proxy for Variability

Our listed catalog of variable sources in Appendix F covers only the sky with overlapping Gaia and ZTF coverage, excluding most of the southern hemisphere. We discuss here an extension of our construction of an all-sky variability index from Hermes et al. (2018) using only data from Gaia DR2, expanding upon the discussion in Section 3.1.

First, we fit an exponential function to our Gaia variability metric, described in Section 3.1, which quantifies Gaia photometric scatter: $V_G = \sigma_G \sqrt{n_{\text{obs},G}} / \langle G \rangle$, where σ_G is the value $\text{PHOT_G_MEAN_FLUX_ERROR}$, $\langle G \rangle$ is the value PHOT_G_MEAN_FLUX , and $n_{\text{obs},G}$ is the value PHOT_G_N_OBS in the Gaia DR2 catalog.

The first exponential fit is shown with the red line in the left-most panel in Figure 14: $\text{Exp1} = (1.35 \times 10^{-8})e^{0.776G} + 0.0096$. In most cases, objects with Gaia variability metrics far from this single exponential fit are excellent candidate variables.

However, we noticed that the residuals to this single exponential function show excess scatter at the faintest magnitudes, shown in the middle panel of Figure 14. This could incorrectly flag some of the faintest white dwarfs as variable. Therefore, we used an additional exponential function that kicked in at magnitudes fainter than $G > 16$ mag in order to follow the bounds of the negative residuals. This choice at $G = 16.0$ mag was motivated by the convergence of the calibrations of the large-scale and small-scale components of the photometric calibration in Gaia DR2 (see especially Figure 9 of Riello et al. (2018)). This second exponential function was fit by eye to the envelope of the unphysical negative residuals, which are only tracing the shape of empirical photometric variability at the faintest magnitudes. This second exponential function is mirrored and shown in blue in the middle panel of Figure 14: $\text{Exp2} = 0.00035e^{G-16.0} + 0.006$.

Subtracting both exponential functions from the Gaia variability metric yields for us a final VARINDEX value, the largest of which ranks for us the highest-probability variables at

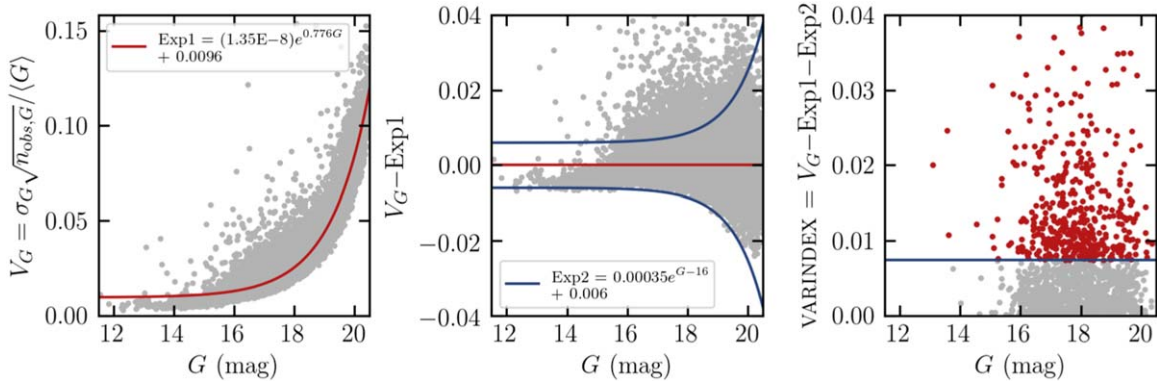


Figure 14. Left: empirical Gaia DR2 variability metric as a function of G -band magnitude, with our first exponential fit delineated in red. Middle: residuals of the first exponential fit, which does not entirely capture the photometric scatter at the faintest magnitudes. A second exponential fit, which kicks in at $G = 16$ mag, is shown in blue, fitted by eye to the negative residuals. Right: final VARINDEX values from the residuals of the two exponential functions, defined in Equation (E1). The 1% most variable objects have VARINDEX >0.0074 and are the objects also marked in red in Figure 1.

all magnitudes for white dwarfs within 200 pc in Gaia DR2. The top 1% most variable white dwarfs are shown in the rightmost panel of Figure 14; the 1% most variable objects have VARINDEX >0.0074 . Our double-exponential calibration should define any object with VARINDEX >0.0 as a strong candidate for variability (see discussion in Section 4.1).

We do not include a catalog of these most variable white dwarfs from only Gaia DR2 photometry, but instead simply include here the relationship for future researchers to duplicate so that they can curate their own variability catalogs directly from the Gaia data:

$$\begin{aligned} \text{varindex}_{\text{DR2}} = & (\text{PHOT_G_MEAN_FLUX_ERROR} \\ & \times \sqrt{\text{PHOT_G_N_OBS}} / \text{PHOT_G_MEAN_FLUX}) \\ & - (1.35 \times 10^{-8} e^{0.776 \text{PHOT_G_MEAN_MAG}} \\ & + 0.00035 e^{\text{PHOT_G_MEAN_MAG} - 16.0} + 0.0156). \end{aligned} \quad (\text{E1})$$

We conclude with the comment that this relationship and these variability catalogs are calibrated for Gaia DR2, and will change slightly with future data releases. We have investigated how this relationship is modified by new photometry and astrometry from the Gaia early data release (eDR3) made public on 2020 December 3 (Gaia Collaboration et al. 2020).

First, we confirm that the majority of white dwarfs from DR2 that were among the top 1% most variable are also in the top 1% using the eDR3 values for their photometric uncertainties.

We have further recalibrated our exponential fits with the new eDR3 photometry, using a method identical to the DR2 procedure outlined in this appendix. That yields the following updated function:

$$\begin{aligned} \text{varindex}_{\text{eDR3}} = & (\text{PHOT_G_MEAN_FLUX_ERROR} \\ & \times \sqrt{\text{PHOT_G_N_OBS}} / \text{PHOT_G_MEAN_FLUX}) \\ & - (8.31 \times 10^{-9} e^{0.794 \text{PHOT_G_MEAN_MAG}} \\ & + 0.0005 e^{\text{PHOT_G_MEAN_MAG} - 17.0} + 0.019). \end{aligned} \quad (\text{E2})$$

Of the 44,045 white dwarfs that are within 200 pc both according to Gaia DR2 and eDR3, the top 1% (top 440) have VARINDEX_{eDR3} >0.0027 . Of those 440 WDs, 284 (65%) were also in the top 1% most variable with the DR2 photometry, and 27 are previously known pulsators. We defer further exploration of the Gaia eDR3 VARINDEX to future work.

Appendix F Table of Top 1% Variable Objects

In Table 5, we show the stellar parameters and metric values for all 121 of the objects in our combined Gaia and ZTF top 1%. A description of columns is found in the note below.

Table 5
Table of Parameters and Metrics for Top 1%

WD	α (deg)	δ (deg)	Class	R	\tilde{V}_{ZTF}	\tilde{V}_G	N_A	G	T_{eff}	$\log(g)$	Observed
WD J001038.25+173907.24	2.65952	17.65175	cZZ	27.7	4.1	9.7	1	17.8	11220	7.9	McD
WD J002511.11+121712.39	6.29599	12.28661	CV	139.7	9.8	25.2	3	17.5	8910	7.3	
WD J002535.80+223741.89	6.39950	22.62813	V	15.2	4.1	3.5	1	18.0	11490	8.1	
WD J004711.37+305609.18	11.79746	30.93552	cZZ	20.1	3.9	6.1	1	17.6	10450	7.5	ZTF
WD J010207.20-003259.57	15.53151	-0.55041	ZZ	14.6	3.3	11.3	0	18.2	10320	7.9	
WD J010528.63+020501.63	16.37012	2.08360	ZZ	15.3	5.6	9.7	0	16.7	11180	7.9	
WD J010749.38+210745.84	16.95550	21.12910	cTR	35.3	7.4	10.2	1	19.2	7590	8.8	McD
WD J013906.17+524536.89	24.77633	52.76027	TR	75.5	7.2	17.9	2	18.5	9420	7.9	McD
WD J014635.73+491443.10	26.64891	49.24527	cCV	51.3	8.0	9.1	2	17.0	8550	8.3	McD
WD J014721.82-215651.39	26.84125	-21.94771	ZZ	73.1	15.8	8.6	2	15.2	10840	8.0	
WD J020158.87-105438.25	30.49558	-10.91064	ZZ	24.3	4.8	19.6	0	16.9	11250	8.1	
WD J021155.07+190631.87	32.97941	19.10887	V	14.9	5.1	9.8	0	18.2	11430	8.1	
WD J022823.31-134726.71	37.09745	-13.79091	V	50.8	10.8	14.6	1	17.0	11530	8.0	
WD J023214.00+344304.51	38.05832	34.71759	V	32.2	5.0	5.8	2	17.0	11230	8.0	
WD J023610.51+223431.86	39.04377	22.57553	cZZ	23.0	2.4	9.2	1	18.4	9660	7.7	McD
WD J024029.66+663637.06	40.12259	66.61015	cZZ	32.1	6.5	9.5	1	15.6	11870	8.0	McD
WD J024927.57+325112.43	42.36522	32.85323	ZZ	17.3	6.2	11.1	0	16.1	11390	8.0	
WD J030648.35-172332.93	46.70206	-17.39228	V	22.1	8.5	13.7	0	16.7	10990	8.0	
WD J032438.66+602055.88	51.16129	60.34886	ZZ	17.9	3.8	2.1	2	16.1	11250	8.0	McD
WD J032833.52-121945.27	52.14013	-12.32930	cTR	23.1	8.4	14.8	0	16.6	8750	8.5	McD
WD J034703.18-180253.49	56.76399	-18.04825	cTR	74.4	14.5	0.3	4	17.4	13370	8.9	McD
WD J034706.79-115808.89	56.77869	-11.96926	ZZ	20.2	11.0	9.1	0	16.0	11670	8.1	
WD J035454.20+074608.59	58.72630	7.76831	V	16.5	7.0	9.5	0	16.6	11190	8.0	
WD J041856.64+271748.31	64.73629	27.29644	ZZ	60.0	19.6	10.4	1	15.1	12380	7.8	
WD J042017.25+361627.27	65.07199	36.27301	ZZ	22.9	13.2	9.7	0	15.7	11270	7.9	
WD J043139.22+192127.77	67.91356	19.35762	V	16.3	3.3	4.8	1	17.5	12560	8.1	
WD J043350.99+485039.18	68.46260	48.84424	ZZ	49.7	9.9	15.0	1	15.9	11370	8.0	McD
WD J044258.31+323715.63	70.74314	32.62089	V	41.2	10.2	10.5	1	17.4	11640	7.9	
WD J044832.11-105349.85	72.13361	-10.89725	ZZ	57.7	6.2	8.2	3	16.3	12250	8.5	McD
WD J045132.19-033308.43	72.88438	-3.55222	ZZ	82.0	11.4	16.0	2	16.1	11290	8.0	McD
WD J045927.24+552521.05	74.86189	55.42159	ZZ	24.4	4.8	19.6	0	16.0	11840	8.0	
WD J050639.84-140511.02	76.66592	-14.08638	V	13.0	9.6	3.4	0	18.2	11180	7.9	
WD J050932.26+450954.98	77.38430	45.16515	V	24.1	5.4	6.7	1	17.5	11030	7.9	
WD J051013.52+043855.13	77.55636	4.64821	ZZ	14.7	8.0	6.7	0	15.4	11780	8.1	
WD J053349.69+155708.02	83.45700	15.95194	V	22.2	4.5	6.6	1	17.6	12020	8.0	
WD J053432.93+770757.40	83.63753	77.13198	MS	22.6	9.1	13.5	0	16.5	10410	8.3	McD
WD J060102.01+541757.82	90.25830	54.29892	cZZ	17.7	4.8	1.2	2	16.7	11110	8.1	McD
WD J062154.74-021605.36	95.47794	-2.26792	cZZ	23.9	4.1	7.9	1	17.4	9490	7.6	McD
WD J062516.34+145558.50	96.31799	14.93281	cZZ	42.9	5.6	8.7	2	17.5	11280	8.1	ZTF
WD J062555.04-141442.31	96.47949	-14.24532	V	23.6	9.7	13.9	0	16.5	8020	8.2	
WD J071839.44+520614.00	109.66381	52.10362	cZZ	34.7	5.7	11.6	1	17.5	11330	8.0	ZTF
WD J073707.98+411227.88	114.28342	41.20747	ZZ	25.1	10.1	15.0	0	15.8	11400	8.1	
WD J082309.66-015246.69	125.78997	-1.87977	V	15.5	6.7	8.8	0	16.9	10790	7.7	
WD J082924.77-163337.25	127.35325	-16.56033	V	19.1	10.9	8.2	0	17.6	11000	8.0	
WD J084007.71+401503.73	130.03140	40.25101	ZZ	13.1	6.7	6.4	0	15.7	11480	8.0	
WD J084652.90+442638.59	131.72060	44.44405	ZZ	13.8	4.1	9.7	0	18.2	11250	8.0	
WD J085507.30+063541.14	133.78021	6.59446	ZZ	15.2	6.5	8.7	0	17.3	10430	7.9	
WD J085722.50-224532.06	134.34310	-22.75867	V	16.3	12.6	3.8	0	15.2	11020	8.0	
WD J091635.08+385546.31	139.14593	38.92932	ZZ	24.6	4.5	7.8	1	16.6	11700	8.1	
WD J091921.84-181719.09	139.84113	-18.28863	V	14.1	5.0	9.1	0	17.6	11620	8.0	
WD J092311.41+423634.16	140.79749	42.60934	cTR	191.4	16.8	2.3	9	17.4	13110	8.0	McD
WD J092351.42+732624.15	140.96430	73.43996	V	1615.5	55.0	45.9	15	18.4	15230	8.5	
WD J093250.57+554315.39	143.21045	55.72102	V	31.0	2.3	13.1	1	17.7	11190	7.9	
WD J104233.54+405715.17	160.64015	40.95423	ZZ	20.4	9.6	10.8	0	16.2	11160	8.0	
WD J104406.25+360046.79	161.02569	36.01279	cZZ	24.1	6.9	5.2	1	17.6	11780	8.2	McD
WD J105010.80-140436.76	162.54415	-14.07693	CV	73.1	14.5	22.0	1	17.2	10260	7.9	
WD J105256.27+130349.55	163.23401	13.06384	V	17.2	7.3	9.9	0	17.4	10380	7.9	
WD J110121.95+401546.36	165.34128	40.26255	V	73.7	9.5	8.9	3	17.5	10750	8.0	
WD J110604.54+180233.72	166.51879	18.04186	cZZ	35.7	10.2	7.7	1	17.5	12610	8.8	McD
WD J114833.63+012859.42	177.13994	1.48316	TR	68.3	14.4	2.7	3	17.2	15310	8.1	
WD J115139.00+265413.46	177.91231	26.90366	V	14.7	3.3	11.4	0	18.1	10900	7.9	
WD J120401.91-065328.98	181.00771	-6.89152	V	22.5	5.1	6.2	1	17.3	11430	8.2	
WD J121924.49-083752.07	184.85179	-8.63114	V	14.3	5.0	9.3	0	17.2	11080	7.8	
WD J121929.50+471522.94	184.87218	47.25636	EB	17.9	1.7	7.2	1	17.6	7410	8.1	
WD J123446.89+164723.47	188.69500	16.78979	V	22.8	4.4	7.0	1	18.2	11170	8.1	

Table 5
(Continued)

WD	α (deg)	δ (deg)	Class	R	\tilde{V}_{ZTF}	\tilde{V}_G	N_A	G	T_{eff}	$\log(g)$	Observed
WD J124804.03+282104.11	192.01683	28.35096	V	15.1	4.7	10.4	0	18.0	11820	8.0	
WD J125009.02+771319.97	192.53681	77.22225	V	15.7	6.9	1.0	1	16.3	15690	8.1	
WD J130110.52+010739.93	195.29393	1.12778	ZZ	55.8	7.4	11.2	2	16.4	11090	7.9	
WD J130957.68+350947.19	197.48913	35.16320	ZZ	13.8	5.8	8.0	0	15.3	11170	8.0	
WD J131246.44-232132.60	198.19216	-23.35931	CV	18.5	8.4	10.1	0	17.7	8820	8.1	
WD J132735.73+190345.90	201.89912	19.06256	V	14.0	5.8	8.2	0	18.2	11380	7.9	
WD J134934.36+280948.93	207.39315	28.16362	V	15.2	9.1	6.1	0	18.5	11240	8.1	
WD J135247.03-044137.04	208.19564	-4.69368	V	14.0	6.6	7.4	0	17.4	11210	7.9	
WD J141126.22+200911.04	212.85905	20.15314	EB	18.2	1.4	1.2	6	17.9	11480	7.9	
WD J141531.30+392357.57	213.87962	39.39944	cZZ	29.7	6.3	8.6	1	17.1	11190	7.9	McD
WD J141708.81+005827.32	214.28655	0.97425	ZZ	13.7	3.5	10.2	0	18.2	10910	7.9	
WD J143047.25+510730.35	217.69666	51.12530	cZZ	17.7	2.6	6.2	1	17.4	11000	8.0	ZTF
WD J144823.77+572454.62	222.09870	57.41506	V	18.0	11.3	6.7	0	17.5	10730	7.9	
WD J145323.52+595056.24	223.34756	59.84885	ZZ	18.9	2.9	6.6	1	17.2	11570	8.0	
WD J145540.89+175351.74	223.92038	17.89776	V	31.7	2.1	8.4	2	17.4	10810	8.0	
WD J150549.19+110506.15	226.45496	11.08485	V	15.1	3.5	11.6	0	18.2	10940	8.0	
WD J152809.27+553914.49	232.03818	55.65448	cZZ	17.9	8.0	9.9	0	17.1	10290	7.5	ZTF
WD J153507.90+252118.56	233.78281	25.35498	V	43.9	7.8	6.8	2	17.6	10380	8.0	
WD J153615.98-083907.53	234.06674	-8.65239	CV	22.5	6.2	16.3	0	18.9	9280	8.0	
WD J154144.89+645352.98	235.43717	64.89778	ZZ	84.6	10.5	17.7	2	15.6	11280	8.0	
WD J155129.23-191418.63	237.87131	-19.23839	V	322.4	19.5	45.0	4	18.1	7240	7.1	
WD J161042.95+503509.05	242.67887	50.58582	V	26.1	2.9	10.1	1	18.1	10550	7.7	
WD J161903.72+091308.96	244.76549	9.21910	V	12.9	9.7	3.2	0	18.2	11210	8.0	
WD J162436.81+321252.81	246.15377	32.21430	cZZ	39.7	8.8	11.1	1	16.7	11200	7.9	McD
WD J162813.34+122452.71	247.05510	12.41426	ZZ	34.5	16.2	18.3	0	16.3	11410	8.0	
WD J163358.75+591206.59	248.49491	59.20201	V	14.1	5.8	8.4	0	17.1	11240	8.0	
WD J163914.29+474835.84	249.80938	47.81017	V	19.6	4.7	14.9	0	17.8	12090	8.1	
WD J170055.38+354951.09	255.23032	35.83057	ZZ	66.8	6.3	15.9	2	17.4	11050	7.9	
WD J171251.78-191550.28	258.21559	-19.26396	cZZ	27.9	10.4	17.5	0	16.3	11910	8.1	McD, CTIO
WD J171840.63+252431.90	259.66923	25.40876	ZZ	218.8	7.1	14.8	9	16.1	11600	8.1	McD
WD J174356.73+443852.18	265.98640	44.64807	V	12.9	2.6	10.3	0	17.3	10620	7.9	
WD J175555.45+395844.68	268.98082	39.97867	cZZ	114.6	8.5	10.6	5	17.0	11300	7.9	McD
WD J181222.75+432107.27	273.09480	43.35229	ZZ	14.8	6.3	8.5	0	16.3	11980	8.5	McD
WD J181728.88+282326.60	274.37059	28.39079	cZZ	72.9	3.2	11.4	4	18.0	10850	8.0	McD
WD J182454.39+344331.58	276.22657	34.72561	cZZ	15.1	1.5	6.0	1	18.3	11890	8.1	ZTF
WD J190024.55+191742.13	285.10238	19.29535	cZZ	86.6	8.6	8.7	4	16.7	11560	8.0	McD
WD J191852.42+583914.09	289.71819	58.65354	cZZ	138.6	13.6	0.3	9	17.4	10750	8.0	McD
WD J200736.50+174214.73	301.90242	17.70399	CV	103.5	24.8	26.9	1	15.2	9760	7.7	
WD J202837.91-060842.77	307.15889	-6.14503	cZZ	38.7	7.8	11.6	1	15.2	11820	8.5	McD
WD J203724.74+570846.01	309.35311	57.14635	V	27.6	6.0	7.8	1	17.2	12660	8.0	
WD J203737.79+323833.34	309.40762	32.64266	cZZ	43.1	8.8	5.6	2	17.5	11480	7.5	
WD J204307.43+121926.72	310.78110	12.32407	V	19.3	3.5	6.1	1	17.9	11800	8.1	
WD J205232.45-011244.62	313.13526	-1.21224	cZZ	37.6	5.2	13.6	1	18.2	11270	7.9	McD
WD J210452.73+233321.42	316.21954	23.55537	ZZ	18.2	7.3	10.9	0	16.0	11250	8.0	
WD J215309.86+461902.53	328.29148	46.31748	cZZ	21.2	2.4	8.3	1	17.8	11620	8.1	McD
WD J220420.60+282321.36	331.08609	28.38937	cZZ	18.1	1.9	7.2	1	17.8	9590	7.4	McD
WD J221945.16-111142.54	334.93837	-11.19500	V	13.9	6.7	7.1	0	18.0	10850	8.0	
WD J225216.48-145907.61	343.06869	-14.98539	V	31.5	4.0	11.7	1	17.5	11310	8.0	
WD J230617.69+243207.68	346.57403	24.53522	ZZ	24.8	10.8	14.0	0	15.4	11530	8.0	
WD J233401.45+392140.87	353.50572	39.36075	CV	206.5	18.0	33.6	3	16.1	7700	7.0	
WD J233921.05+512410.79	354.83814	51.40253	cZZ	18.9	8.3	10.5	0	16.8	11070	7.9	ZTF
WD J234830.32+415424.54	357.12632	41.90679	V	21.3	3.8	6.8	1	18.1	11130	7.9	
WD J234949.49+225014.76	357.45643	22.83699	cZZ	43.1	8.5	13.0	1	17.6	12130	8.1	McD
WD J234953.46+130612.92	357.47404	13.10378	cZZ	29.3	4.6	5.1	2	16.1	10660	7.9	McD
WD J235010.39+201914.37	357.54317	20.32053	cZZ	15.2	2.3	12.9	0	17.4	11870	8.0	ZTF
WD J235915.98+653225.97	359.81627	65.54060	V	18.8	4.3	5.1	1	18.0	12330	8.1	

Note. Description of columns: all of the object names and stellar parameters are directly sourced from the Gentile Fusillo et al. (2019) Gaia DR2 catalog for candidate white dwarfs. Here, α and δ are the J2015.5 Gaia R.A. and decl. in degrees, G is the average observed Gaia G-band magnitude, and T_{eff} (K) and $\log(g)$ (dex) are derived from the Gaia photometry assuming a pure hydrogen photosphere. The rank parameter, R , and individual variability metric values for each object are also presented. We use the Observatory column to indicate which objects were followed up with the McDonald Observatory 2.1 m telescope (McD; see Appendix C), the CTIO SMARTS 0.9 m (CTIO; see Appendix D), and the eight new ZZ Ceti classified using their ZTF light curves (ZTF). The key for these classifications is as follows: ZZ = known ZZ Ceti, cZZ = new confirmed ZZ Ceti, CV = known cataclysmic variable, cCV = new confirmed cataclysmic variable, TR = known transiting debris, cTR = new candidate white dwarf with transiting debris, EB = known eclipsing binary, MS = rotational modulation due to a cool magnetic spot, and V are objects whose variability has yet to be classified or confirmed.

Appendix G

Table of Pulsation Spectra for Newly Confirmed ZZ Ceti with Follow-up Photometry

Motivated by Mukadam et al. (2006), we catalog here in Table 6 the linearly independent peaks greater than the $4\langle A \rangle$ significance threshold from our follow-up high-speed photometric observations using the 2.1 m Otto Struve telescope at McDonald Observatory in the *BG40* bandpass filter (unless specified otherwise) and the 0.9 m SMARTS telescope at Cerro Telolo Inter-American Observatory in the *V*-band. Linearly independent peaks were determined by using the prewhitening tools provided by the PYRIOD Python package. We present the

periodicities in descending order by amplitude. The weighted mean period (WMP) of these pulsations for each object is also presented.

We also report all the linearly independent periods in the ZTF time series with amplitudes greater than the 0.1% false alarm probability significance thresholds we estimated from our bootstrapping exercise for the objects in the top 1%. We distinguish these periodicities by the ZTF light curves: *g*, *r*, and the combined *g+r* light curve. While most of these periods are characteristic of ZZ Ceti pulsations, we denote objects that are known nonpulsators or whose periodicities are not indicative of pulsations with a ‡ in the WMP column, to avoid confusion.

Table 6
Pulsation Spectra for Newly Confirmed ZZ Ceti









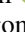
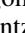
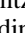
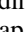

WD	T_{eff} (K)	$\log(g)$ (cgs)	WMP (s)	Linearly Independent Modes: Period/Amplitude (s)/(%)
McDonald 2.1 m Pulsators				
WD J001038.25+173907.24	11220	7.9	855.9	978.2/3.4, 702.0/2.7
WD J023610.51+223431.86	9660	7.7	812.4	831.7/4.3, 898.5/3.2, 618.6/1.5, 579.2/1.1, 990.9/1.0
WD J024029.66+663637.06	11870	8.0	411.2	864.5/2.0, 982.9/1.0, 1058.2/0.9, 623.9/0.4
WD J032438.66+602055.88	11250	8.0	797.5	818.3/2.0, 894.1/0.8, 691.8/0.7, 999.5/0.7, 506.7/0.6
WD J043350.99+485039.18	11370	8.0	549.5	510.6/3.1, 583.7/2.8, 464.2/1.6, 667.2/1.4
WD J044832.11−105349.85	12250	8.5	508.0	536.4/5.3, 316.8/0.8
WD J045132.19−033308.43	11290	8.0	839.5	831.3/3.0, 908.8/2.3, 751.7/1.5
WD J060102.01+541757.82	11110	8.1	861.5	861.5/0.3
WD J062154.74−021605.36†	9490	7.6	767.8	788.5/2.0, 874.9/1.8, 645.5/1.6, 510.5/1.5, 1095.5/1.0
WD J104406.25+360046.79	11780	8.2	628.6	661.6/1.6, 361.8/1.5, 897.5/1.3
WD J110604.54+180233.72	12610	8.8	417.4	369.7/10.2, 1180.2/0.6, 537.2/0.5
WD J141531.30+392357.57	11190	7.9	786.5	953.6/4.3, 735.3/2.9, 710.8/2.6, 399.6/1.0
WD J162436.81+321252.81	11200	7.9	845.6	930.2/6.0, 648.1/2.6
WD J171251.78−191550.28	11910	8.1	574.2	569.9/5.4, 488.7/3.1, 762.7/2.3, 455.0/1.2
WD J171840.63+252431.90	11600	8.1	481.1	494.0/3.6, 397.3/1.2, 531.9/1.0
WD J175555.45+395844.68	11300	7.9	780.7	920.8/2.5, 530.5/2.2, 656.5/1.7, 1286.8/0.8
WD J181222.75+432107.27	11980	8.5	556.8	407.2/3.7, 788.7/1.7, 741.4/1.4, 476.6/1.2
WD J181728.88+282326.60	10850	8.0	614.2	581.4/4.0, 464.9/1.1, 747.2/1.0, 811.4/0.8
WD J184424.33+504727.95	*	*	3700.6	4188.2/6.4, 2922.9/1.7, 1863.2/1.0
WD J190024.55+191742.13	11560	8.0	483.8	507.2/4.1, 546.3/1.7, 285.6/0.8, 401.3/0.6
WD J191852.42+583914.09	10750	8.0	1192.8	1099.7/0.9, 997.3/0.8, 1497.3/0.4, 861.3/0.4, 1952.8/0.3
WD J202837.91−060842.77	11820	8.5	696.2	526.5/1.9, 412.6/1.7, 703.9/1.3, 1987.2/0.7, 587.8/0.4
WD J203737.79+323833.34	11480	7.5	1326.4	1296.2/4.3, 1016.3/3.2, 1661.5/2.7, 1769.8/2.5, 1126.5/1.7, 922.4/1.4
WD J205232.45−011244.62	11270	7.9	784.4	882.4/7.0, 626.5/1.9, 518.1/1.4
WD J215309.86+461902.53	11620	8.1	719.3	646.9/2.5, 907.3/2.5, 830.1/1.7, 502.9/1.4, 586.1/1.3
WD J220420.60+282321.36	9590	7.4	735.5	532.1/2.8, 932.3/2.2, 566.7/1.6, 476.1/0.8, 1277.5/0.7, 1172.0/0.5
WD J234953.46+130612.92	10660	7.9	1049.7	1078.1/1.9, 1166.5/1.4, 990.4/0.9, 775.9/0.9, 1533.6/0.6, 834.2/0.4, 739.5/0.4
WD J234949.49+225014.76	12130	8.1	867.4	872.7/9.4, 532.8/2.0, 1265.4/1.5
CTIO 0.9 m Pulsators				
WD J100223.96−575507.91	12110	8.0	747.0	708.5/2.5, 805.4/1.6
WD J111221.43−513003.90	11190	8.0	788.7	764.9/3.9, 828.0/2.3
WD J115414.55−592658.81	11170	8.0	890.5	890.5/3.5
WD J171251.78−191550.28	11910	8.1	522.8	570.4/4.3, 490.5/3.3, 455.0/1.4
WD J174349.28−390825.95	11560	8.1	763.0	785.3/3.0, 605.7/2.5, 871.7/2.2, 732.1/2.0, 488.9/1.4, 680.9/1.4, 1492.1/0.9
WD J204349.21−390318.02	11270	8.0	773.4	857.5/1.9, 940.3/0.9, 694.2/0.5, 486.4/0.4, 366.4/0.4
WD J211815.52−531322.72	11120	7.9	943.4	943.4/2.4
WD J224840.07−064244.65	11640	8.1	529.8	558.3/3.7, 481.7/2.2
ZTF Significant Periods				
WD J004711.37+305609.18	10450	7.5	813.1	<i>r</i> : 940.9/2.1; <i>g+r</i> : 940.9/2.2, 618.7/1.7 (4.66 $\langle A \rangle$)
WD J010528.63+020501.63	11180	7.9	453.6	<i>g+r</i> : 453.6/2.0 (4.96 $\langle A \rangle$)
WD J014635.73+491443.10	8550	8.3	‡	<i>r</i> : 7407.7/8.5; <i>g+r</i> : 7407.7/4.9 (5.07 $\langle A \rangle$)

Table 6
(Continued)

WD	T_{eff} (K)	$\log(g)$ (cgs)	WMP (s)	Linearly Independent Modes: Period/Amplitude (s)/(%)
WD J024029.66+663637.06	11870	8.0	542.3	$g+r$: 542.3/1.6 (4.96 $\langle A \rangle$)
WD J041856.64+271748.31	12380	7.8	516.9	$g+r$: 537.7/2.8, 494.2/2.1 (4.63 $\langle A \rangle$)
WD J053432.93+770757.40	10410	8.3	‡	g : 2604.5/7.6, 1302.2/1.8; r : 2604.5/3.6, 1302.2/1.6; $g+r$: 2604.5/5.2, 1302.2/1.6 (5.01 $\langle A \rangle$)
WD J062516.34+145558.50	11280	8.1	831.5	r : 836.6/2.4, 610.6/1.9; $g+r$: 832.4/1.8, 582.0/1.5, 979.1/1.4 (4.34 $\langle A \rangle$)
WD J062555.04-141442.31	8020	8.2	‡	g : 13542.1/5.5; r : 13541.9/4.6; $g+r$: 13542.0/5.0 (4.86 $\langle A \rangle$)
WD J071839.44+520614.00	11330	8.0	627.4	$g+r$: 627.4/2.2 (4.95 $\langle A \rangle$)
WD J091635.08+385546.31	11700	8.1	476.1	$g+r$: 498.1/2.2, 451.9/1.7 (5.00 $\langle A \rangle$)
WD J121929.50+471522.94	7410	8.1	‡	g : 54949.0/3.0; r : 54959.6/2.5; $g+r$: 54953.6/2.6 (5.11 $\langle A \rangle$)
WD J141531.30+392357.57	11190	7.9	1002.9	$g+r$: 1002.9/1.2 (4.59 $\langle A \rangle$)
WD J145323.52+595056.24	11570	8.0	458.1	g : 458.1/3.0; r : 458.1/2.5; $g+r$: 458.1/2.8 (5.02 $\langle A \rangle$)
WD J152809.27+553914.49	10290	7.5	769.1	g : 769.1/2.7; r : 769.1/1.9; $g+r$: 769.1/2.1 (5.09 $\langle A \rangle$)
WD J170055.38+354951.09	11050	7.9	696.5	g : 508.0/2.1, 558.8/1.8; r : 555.2/1.5, 646.3/1.2, 514.1/1.1; $g+r$: 555.2/1.6, 508.0/1.6, 891.8/1.0 (4.33 $\langle A \rangle$)
WD J171251.78-191550.28	11910	8.1	528.3	r : 573.8/3.9, 488.6/2.6, 261.5/1.4, 287.9/1.3, 746.1/1.1, 447.2/1.1; $g+r$: 573.8/3.8, 485.8/2.5, 259.1/1.5, 449.5/1.2, 752.7/1.2, 290.7/1.1 (4.07 $\langle A \rangle$)
WD J171840.63+252431.90	11600	8.1	481.7	g : 495.2/2.3, 397.5/1.4, 532.1/1.1; r : 495.2/1.8, 401.2/0.9; $g+r$: 495.2/2.0, 397.5/1.2, 532.1/0.9 (4.59 $\langle A \rangle$)
WD J175555.45+395844.68	11300	7.9	701.2	$g+r$: 701.2/1.4 (5.06 $\langle A \rangle$)
WD J181222.75+432107.27	11980	8.5	353.4	$g+r$: 353.4/1.2 (4.96 $\langle A \rangle$)
WD J181728.88+282326.60	10850	8.0	608.9	$g+r$: 585.0/1.8, 631.0/1.7 (4.89 $\langle A \rangle$)
WD J190024.55+191742.13	11560	8.0	510.4	g : 510.4/3.1; $g+r$: 510.4/2.3 (4.90 $\langle A \rangle$)
WD J200736.50+174214.73	9760	7.7	‡	g : 2520.5/6.3; r : 2448.9/6.0, 64954.5/3.4, 1569.9/2.5; $g+r$: 2448.9/6.1, 263876.6/3.0, 1540.5/2.2 (5.20 $\langle A \rangle$)
WD J215309.86+461902.53	11620	8.1	942.9	r : 921.1/1.7; $g+r$: 942.9/1.4 (5.02 $\langle A \rangle$)
WD J233401.45+392140.87	7700	7.0	‡	g : 2432.6/4.0; r : 4823.2/3.7, 2432.6/3.3; $g+r$: 2432.6/3.7, 4823.2/2.8 (4.92 $\langle A \rangle$)
WD J233921.05+512410.79	11070	7.9	1050.6	r : 1037.4/1.6; $g+r$: 1050.6/1.3 (4.74 $\langle A \rangle$)
WD J235010.39+201914.37	11870	8.0	364.2	g : 365.7/2.4; r : 364.2/1.5; $g+r$: 364.2/1.8 (4.84 $\langle A \rangle$)

Note. *—The lowest-mass ELM white dwarfs do not have T_{eff} and $\log(g)$ values in the Gentile Fusillo et al. (2019) Gaia DR2 catalog. †—Observed in SDSS g -band. ‡—The weighted mean period of pulsations is only relevant to pulsating white dwarfs.

ORCID iDs

Joseph A. Guidry  <https://orcid.org/0000-0001-9632-7347>
 Zachary P. Vanderbosch  <https://orcid.org/0000-0002-0853-3464>
 J. J. Hermes  <https://orcid.org/0000-0001-5941-2286>
 Brad N. Barlow  <https://orcid.org/0000-0002-8558-4353>
 Isaac D. Lopez  <https://orcid.org/0000-0002-0009-409X>
 Thomas M. Boudreaux  <https://orcid.org/0000-0002-2600-7513>
 Kyle A. Corcoran  <https://orcid.org/0000-0002-2764-7248>
 Keaton J. Bell  <https://orcid.org/0000-0002-0656-032X>
 M. H. Montgomery  <https://orcid.org/0000-0002-6748-1748>
 Tyler M. Heintz  <https://orcid.org/0000-0003-3868-1123>
 Joshua S. Reding  <https://orcid.org/0000-0003-1862-2951>
 Bart H. Dunlap  <https://orcid.org/0000-0002-1086-8685>
 D. E. Winget  <https://orcid.org/0000-0003-0181-2521>

References

- Andrew, S., Swihart, S. J., & Strader, J. 2021, *ApJ*, **908**, 180
 Astropy Collaboration, Price-Whelan, A. M., Sipőcz, B. M., et al. 2018, *AJ*, **156**, 123
 Astropy Collaboration, Robitaille, T. P., Tollerud, E. J., et al. 2013, *A&A*, **558**, A33
 Bailer-Jones, C. A. L., Rybizki, J., Fousneau, M., Mantelet, G., & Andrae, R. 2018, *AJ*, **156**, 58
 Bell, K. J. 2020, AAS Meeting, **235**, 106.06
 Bell, K. J., Córscico, A. H., Bischoff-Kim, A., et al. 2019, *A&A*, **632**, A42
 Bell, K. J., Hermes, J. J., Bischoff-Kim, A., et al. 2015, *ApJ*, **809**, 14
 Bell, K. J., Hermes, J. J., Montgomery, M. H., et al. 2016, *ApJ*, **829**, 82
 Bellm, E. C., Kulkarni, S. R., Barlow, T., et al. 2019, *PASP*, **131**, 068003
 Belloni, D., Schreiber, M. R., Pala, A. F., et al. 2020, *MNRAS*, **491**, 5717
 Bida, T. A., Dunham, E. W., Massey, P., & Roe, H. G. 2014, *Proc. SPIE*, **9147**, 91472N
 Bognár, Z., Kawaler, S. D., Bell, K. J., et al. 2020, *A&A*, **638**, A82
 Bognár, Z., & Sodor, A. 2016, *IBVS*, **6184**, 1
 Bradley, L., Sipőcz, B., Robitaille, T., et al. 2020, *astropy/photutils*: 1.0.0, Zenodo, doi:10.5281/zenodo.4044744
 Brandner, W., Zinnecker, H., & Kopytova, T. 2021, *MNRAS*, **500**, 3920
 Busso, G., Cacciari, C., Carrasco, J. M., et al. 2018, Gaia DR2 Documentation, European Space Agency and Gaia Data Processing and Analysis Consortium, <https://gea.esac.esa.int/archive/documentation/GDR2/>
 Carrasco, J. M., Evans, D. W., Montegriffo, P., et al. 2016, *A&A*, **595**, A7
 Castanheira, B. G., Kepler, S. O., Kleinman, S. J., Nitta, A., & Fraga, L. 2010, *MNRAS*, **405**, 2561
 Chambers, K. C., Magnier, E. A., Metcalfe, N., et al. 2016, arXiv:1612.05560
 Chen, X., Wang, S., Deng, L., et al. 2020, *ApJS*, **249**, 18
 Chonis, T. S., Hill, G. J., Lee, H., et al. 2016, *Proc. SPIE*, **9908**, 99084C
 Clemens, J. C. 1993, *BaltA*, **2**, 407
 Coughlin, M. W., Burdge, K., Duev, D. A., et al. 2020, arXiv:2009.14071
 Currie, M. J., Berry, D. S., Jenness, T., et al. 2014, in ASP Conf. Ser. 485, Astronomical Data Analysis Software and Systems XXIII, ed. N. Manset & P. Forshay (San Francisco, CA: ASP), 391
 Dame, K., Belardi, C., Kilic, M., et al. 2019, *MNRAS*, **490**, 1066
 Debes, J. H., Walsh, K. J., & Stark, C. 2012, *ApJ*, **747**, 148
 Dye, S., Lawrence, A., Read, M. A., et al. 2018, *MNRAS*, **473**, 5113
 Evans, D. W., Riello, M., De Angeli, F., et al. 2018, *A&A*, **616**, A4
 Eyer, L., Rimoldini, L., Rohrbasser, L., et al. 2020, in Proc. of the Conf. Stars and their Variability Observed from Space, ed. C. Neiner et al. (Vienna: Univ. Vienna), 11

- Faedi, F., West, R. G., Burleigh, M. R., Goad, M. R., & Hebb, L. 2011, *MNRAS*, **410**, 899
- Fantini, N. J., Côté, P., & McConnachie, A. W. 2020, *ApJ*, **900**, 139
- Farihi, J. 2016, *NewAR*, **71**, 9
- Ferrario, L., Bailey, J., & Wickramasinghe, D. 1996, *MNRAS*, **282**, 218
- Flewelling, H. A., Magnier, E. A., Chambers, K. C., et al. 2020, *ApJS*, **251**, 7
- Fulton, B. J., Tonry, J. L., Flewelling, H., et al. 2014, *ApJ*, **796**, 114
- Gaia Collaboration, Brown, A. G. A., Vallenari, A., et al. 2018, *A&A*, **616**, A1
- Gaia Collaboration, Brown, A. G. A., Vallenari, A., et al. 2020, arXiv:2012.01533
- Gaia Collaboration, Eyer, L., Rimoldini, L., et al. 2019, *A&A*, **623**, A110
- Gänsicke, B. T., Aungwerojwit, A., Marsh, T. R., et al. 2016, *ApJL*, **818**, L7
- Gentile Fusillo, N. P., Tremblay, P.-E., Gänsicke, B. T., et al. 2019, *MNRAS*, **482**, 4570
- Gianninas, A., Kilic, M., Brown, W. R., Canton, P., & Kenyon, S. J. 2015, *ApJ*, **812**, 167
- Graham, M. J., Kulkarni, S. R., Bellm, E. C., et al. 2019, *PASP*, **131**, 078001
- Greiss, S., Gänsicke, B. T., Hermes, J. J., et al. 2014, *MNRAS*, **438**, 3086
- Hallakoun, N., Xu, S., Maoz, D., et al. 2017, *MNRAS*, **469**, 3213
- Harris, C. R., Millman, K. J., van der Walt, S. J., et al. 2020, *Natur*, **585**, 357
- Hermes, J., Corcoran, K. A., Boudreaux, T. M., et al. 2018, A Method to Select Variable White Dwarfs from Gaia DR2, 21st European White Dwarf Workshop, Zenodo, doi:10.5281/zenodo.4088554
- Hermes, J. J., Gänsicke, B. T., Gentile Fusillo, N. P., et al. 2017a, *MNRAS*, **468**, 1946
- Hermes, J. J., Gänsicke, B. T., Kawaler, S. D., et al. 2017b, *ApJS*, **232**, 23
- Hermes, J. J., Montgomery, M. H., Bell, K. J., et al. 2015, *ApJL*, **810**, L5
- Hermes, J. J., Montgomery, M. H., Gianninas, A., et al. 2013, *MNRAS*, **436**, 3573
- Holl, B., Audard, M., Nienartowicz, K., et al. 2018, *A&A*, **618**, A30
- Horne, K. 1986, *PASP*, **98**, 609
- Hunter, J. D. 2007, *CSE*, **9**, 90
- Izquierdo, P., Rodríguez-Gil, P., Gänsicke, B. T., et al. 2018, *MNRAS*, **481**, 703
- Jackman, J. A. G., Wheatley, P. J., Bayliss, D., et al. 2019, *MNRAS*, **485**, L136
- Ivezić, Ž., Kahn, S. M., Tyson, J. A., et al. 2019, *ApJ*, **873**, 111
- Kanaan, A., Kepler, S. O., & Winget, D. E. 2002, *A&A*, **389**, 896
- Kawka, A., Simpson, J. D., Vennes, S., et al. 2020, *MNRAS*, **495**, L129
- Kepler, S. O., Pelisoli, I., Koester, D., et al. 2015, *MNRAS*, **446**, 4078
- Kepler, S. O., Pelisoli, I., Koester, D., et al. 2019, *MNRAS*, **486**, 2169
- Kilic, M., Gianninas, A., Bell, K. J., et al. 2015, *ApJL*, **814**, L31
- Kleinman, S. J., Kepler, S. O., Koester, D., et al. 2013, *ApJS*, **204**, 5
- Koester, D. 2010, *MmSAI*, **81**, 921
- Landolt, A. U. 1968, *ApJ*, **153**, 151
- Lindgren, L., Hernández, J., Bombrun, A., et al. 2018, *A&A*, **616**, A2
- Lomb, N. R. 1976, *Ap&SS*, **39**, 447
- Marsh, T. R. 1989, *PASP*, **101**, 1032
- Masci, F. J., Laher, R. R., Rusholme, B., et al. 2019, *PASP*, **131**, 018003
- Mowlavi, N., Rimoldini, L., Evans, D. W., et al. 2021, *A&A*, **648**, A44
- Mukadam, A. S., Bischoff-Kim, A., Fraser, O., et al. 2013, *ApJ*, **771**, 17
- Mukadam, A. S., Montgomery, M. H., Winget, D. E., Kepler, S. O., & Clemens, J. C. 2006, *ApJ*, **640**, 956
- Mukadam, A. S., Mullally, F., Nather, R. E., et al. 2004, *ApJ*, **607**, 982
- Mustill, A. J., & Villaver, E. 2012, *ApJ*, **761**, 121
- Newville, M., Stensitzki, T., Allen, D. B., & Ingargiola, A. 2014, LMFIT: Non-Linear Least-Square Minimization and Curve-Fitting for Python, 0.8.0, Zenodo, doi:10.5281/zenodo.11813
- Pala, A. F., Gänsicke, B. T., Breedt, E., et al. 2020, *MNRAS*, **494**, 3799
- pandas development team T. 2020, pandas-dev/pandas: Pandas, latest, Zenodo, doi:10.5281/zenodo.3509134
- Patterson, M. T., Bellm, E. C., Rusholme, B., et al. 2019, *PASP*, **131**, 018001
- Rappaport, S., Gary, B. L., Kaye, T., et al. 2016, *MNRAS*, **458**, 3904
- Rappaport, S., Gary, B. L., Vanderburg, A., et al. 2018, *MNRAS*, **474**, 933
- Rappaport, S., Levine, A., Chiang, E., et al. 2012, *ApJ*, **752**, 1
- Riello, M., De Angeli, F., Evans, D. W., et al. 2018, *A&A*, **616**, A3
- Romero, A. D., Córscico, A. H., Althaus, L. G., et al. 2012, *MNRAS*, **420**, 1462
- Rowan, D. M., Tucker, M. A., Shappee, B. J., & Hermes, J. J. 2019, *MNRAS*, **486**, 4574
- Sandhaus, P. H., Debes, J. H., Ely, J., Hines, D. C., & Bourque, M. 2016, *ApJ*, **823**, 49
- Scargle, J. D. 1982, *ApJ*, **263**, 835
- Tremblay, P. E., Bergeron, P., & Gianninas, A. 2011, *ApJ*, **730**, 128
- Tremblay, P. E., Cummings, J., Kalirai, J. S., et al. 2016, *MNRAS*, **461**, 2100
- van Lieshout, R., Min, M., Dominik, C., et al. 2016, *A&A*, **596**, A32
- van Sluijs, L., & Van Eylen, V. 2018, *MNRAS*, **474**, 4603
- Vanderbosch, Z., Hermes, J. J., Dennihy, E., et al. 2020, *ApJ*, **897**, 171
- Vanderburg, A., Johnson, J. A., Rappaport, S., et al. 2015, *Natur*, **526**, 546
- Vanderburg, A., Rappaport, S. A., Xu, S., et al. 2020, *Natur*, **585**, 363
- VanderPlas, J. T. 2018, *ApJS*, **236**, 16
- Vincent, O., Bergeron, P., & Lafrenière, D. 2020, *AJ*, **160**, 252
- Wallach, A., Morris, B. M., Branton, D., et al. 2018, *RNAAS*, **2**, 41
- Winget, D. E., Nather, R. E., Clemens, J. C., et al. 1994, *ApJ*, **430**, 839
- Witham, A. R., Knigge, C., Gänsicke, B. T., et al. 2006, *MNRAS*, **369**, 581
- Xu, S., Hallakoun, N., Gary, B., et al. 2019, *AJ*, **157**, 255